Research Article

High Precision Control of Rotating Payload Satellite considering Static and Dynamic Unbalanced Disturbance

Yatao Zhao, Cheng Wei , Qingsheng Wei, and Yang Zhao

School of Astronautics, Harbin Institute of Technology, Harbin 150001, China

Correspondence should be addressed to Cheng Wei; weicheng@hit.edu.cn

This paper is devoted to suppressing the lumped disturbance, which is mainly composed of static and dynamic unbalanced disturbance, to ensure the imaging quality of the rotating payload satellite system with a five-degree-of-freedom active magnetic bearing. The dynamic model of lumped disturbance in imaging phase is established to design the balancing error index of payload unbalance, and the effect of bearing mechanical characteristics is analyzed. A novel fixed-time extended state observer is proposed to estimate unknown lumped disturbance and uncertainty. On this basis, a novel quaternion-based fixed-time nonsingular terminal sliding mode controller is presented to achieve high precision, high stability, and chattering-free attitude control. The complete proof on the faster convergence performance of the presented sliding mode surface compared to the existing sliding mode surfaces and the fixed-time convergence of the presented controller is provided. Numerical simulation results are carried out to verify the lumped disturbance modeling accuracy and the effectiveness of the proposed controller.

1. Introduction

In earth observation missions, remote sensing images acquired by optical observation payloads are widely used in military and civil fields because of their wide coverage and rich spectral bands. The imaging coverage capability is an important index of optical remote sensing satellites, and its demand is increasing to obtain more information per unit time. However, the relationship between high resolution and wide field of view is contradictory. In the traditional push-broom imaging mode, in order to increase the field of view width on the basis of ensuring the imaging resolution, the common methods are inner field of view stitching [1] and external field of view stitching [2, 3]. However, these methods are difficult to implement due to the limitations of production process, development cost, and satellite carrying capacity, and the improvement of imaging width is limited.

To further increase the imaging width, a novel spin-scan imaging mode is proposed in [4], where the optical payload is installed on the axial direction of the satellite platform, and the optical axis is perpendicular to the advancing direction of the satellite. When the payload rotates relative to the satellite platform, a larger stripe-size area can be obtained. In addition, since the advantages of longer life, no wear, no lubrication, and higher rotational speed [5, 6], the five degree-of-freedom active magnetic bearing (5-DOF AMB) is utilized as a connecting element between the payload and the platform instead of conventional mechanical bearing to improve the rotational accuracy of payload. The specific structure of the rotating payload satellite (denoted as RPS) can be found in [7]. Note that the mass and inertia of the payload considered in the RPS system are comparable to the satellite platform.

In practice, the operational phases of the RPS system are complex. The satellite platform has two phases: attitude maneuvering phase and earth orientation phase, the rotating payload has three phases: spin-up phase, constant-speed rotation phase, and despinning phase. When the satellite platform maintains earth orientation and the payload keeps rotating at a constant speed, the payload enters the remote sensing imaging mode, denoted as the imaging phase, with

the demand of high attitude accuracy and stability, which is the concern of this paper.

However, the large mass payload is unbalanced due to production and assembly errors and cannot be completely compensated by the existing balancing technology [8]. The payload unbalance consists of static unbalance and dynamic unbalance, where the former is related to the centroid deviation relative to the rotation axis, and the latter is related to the inertia product. When the large mass payload rotates, static unbalanced disturbance, dynamic unbalanced disturbance, and inertia difference disturbance caused by the radial principal inertia difference of the payload and axial angular momentum disturbance are transmitted to the satellite platform through the AMB. The abovementioned multiple disturbances are collectively referred to as lumped disturbance, which stimulate the nutation motion of the RPS system and seriously affect the control accuracy of payload in the imaging phase. In addition, the dynamic unbalance and static unbalance of the payload are randomly valued within the error boundary and change in orbit, indicating that the lumped disturbance is unknown in practice, which makes the suppression of the lumped disturbance complicated.

To suppress the disturbance effect, the maximum torque of the actuator needs to be greater than the boundary of the lumped disturbance with a certain margin. However, due to the complex composition of lumped disturbance and the mechanical characteristics of the AMB, modeling the lumped disturbance in the imaging phase is a challenging problem. Furthermore, plenty of related research works have focused on controller design with disturbance, uncertainty, and nonlinearity, including the model predictive control [9], the robust H-infinity control [10, 11], and the active disturbance rejection control [12, 13]. Moreover, the sliding mode control (SMC) has been widely used in satellite attitude control due to its high accuracy and strong robustness against disturbances [14–16]. However, the above sliding mode controllers drive the system states to the equilibrium point asymptotically in infinite time, which cannot meet the requirement of rapid stability. Therefore, the research on finite-time sliding mode control for satellite attitude using terminal sliding mode (TSM) surface [17] has been carried out, which can make the system states converge to the equilibrium with a finite settling time and better resistance to disturbances. Recent researches on finite-time sliding mode control have focused on designing sliding mode surface with faster convergence rate, such as fast terminal sliding mode (FTSM) surface [18–20], and solving inherent singular problem, such as nonsingular TSM surface [21, 22] and nonsingular FTSM surface [23–25]. However, finite-time stability theory cannot guarantee that the system states converge within a bounded time independent of the initial values, and the convergence time cannot be estimated when the initial values are unknown. Fixed-time sliding mode control, with faster convergence speed and higher control accuracy, ensures that the convergence time is bounded regardless of the initial values and has been widely studied in [26–29], where the convergence speed of the utilized sliding mode surfaces gradually increase and the singularity problem is avoided.

The requirement of disturbance's boundary and the chattering phenomenon are the two main drawbacks of SMC that need to be improved. When the disturbance boundary is unknown, the switching gain needs to be selected sufficiently large to ensure the stability and adaptability of the controller, resulting in large energy consumption [30] and aggravating the chattering phenomenon. Although the maximum torque of the actuator can be used as the boundary in this paper, it is still conservative. In order to obtain the true boundary of disturbance to attenuate the chattering, an adaptive law can be adopted to adjust the switching gain, denoted as adaptive SMC, and uses the continuous function [17, 20, 28, 29] or boundary layer method [24, 31] to replace the discontinuous term in the controller, which is an effective way to improve the SMC's drawbacks. But in the references [18, 24, 25, 31, 32] of adaptive SMC, the system states are only practically finite-time or fixed-time stable. In addition, utilizing disturbance observer algorithm to estimate and compensate disturbance to further improve control accuracy is an alternative solution [19, 30, 33, 34], where the switching gain needs to be greater than zero instead of disturbance's boundary, or directly omitted, achieving chattering-free control while ensuring the system states are finite-time or fixed-time stable.

According to the above discussion, there are two research objectives in this paper. First, establish the dynamic model of lumped disturbance in the imaging phase, and then, the disturbance analysis is studied. Second, in order to improve the attitude accuracy and stability of the payload in the presence of unknown lumped disturbance and uncertainty, a novel quaternion-based fixed-time nonsingular fast terminal sliding mode control (QFNFTSMC) is proposed as the controller for the satellite platform. In the proposed controller, a novel quaternion-based fixed-time nonsingular fast terminal sliding mode surface (QFNFTSMS) and a novel fixed-time extended state observer (FESO) are utilized. To the best knowledge of the authors, there are few studies on the dynamic model and attitude controller of the RPS system with 5-DOF AMB. The main contributions of this paper can be summarized as follows:

(1) The dynamic model of the lumped disturbance is established, and the disturbance analysis including the balancing error index, actuator selection, and the effect of AMB mechanical characteristics is carried out

(2) A proof of the fast convergence performance of the novel QFNFTSMS compared to other sliding mode surfaces is given, and a complete proof of fixed-time convergence of the states on the QFNFTSMS is proposed

(3) Based on FESO algorithm, a novel QFNFTSMC is proposed to achieve high precision, high stability, and chattering-free attitude control of the RPS system in the presence of unknown lumped disturbance and uncertainty

The rest of this paper is organized as follows. In Section 2, the dynamic model of the RPS system and the dynamic

model of lumped disturbance are proposed, followed by a brief disturbance analysis. The quaternion-based fixed-time nonsingular fast terminal sliding mode control with sliding mode surface and extended state observer is presented in Section 3. Simulations and results are given in Section 4. Lastly, the conclusion obtained in this paper is summarized in Section 5.

2. Modeling of RPS System

As shown in Figure 1, the RPS system consists of platform subsystem, payload subsystem, and AMB subsystem. The platform subsystem consists of a satellite platform, solar panels, and a wheel control system, and the payload subsystem consists of a large mass rotating payload and a single-axis momentum wheel used to control the axial rotation speed of the payload relative to the satellite platform.

The AMB subsystem is used to connect the platform subsystem and the payload subsystem. As shown in Figure 2, the AMB consists of a thrust active magnetic bearing (TAMB), a shaft, a touchdown bearing (TB), eddy-current position sensors, and two identical radial active magnetic bearings (RAMBs), where the one near the satellite platform is noted as the left RAMB, and the one near the rotating payload is noted as the right RAMB. The shaft with a thrust disk is fixed on the rotating payload to form the AMB rotor; RAMBs and TAMB are fixed on the satellite platform to form the AMB stator, where the RAMB is configured with two magnetic pole pairs to provide radial displacement stiffness and angular stiffness; the TAMB is configured with a pair of annular magnetic poles to provide axial displacement stiffness. When the rotor moves relative to the stator, the position sensors detect the air gap changes of each magnetic pole pair; then, the RAMB generates radial electromagnetic force and the TAMB generates axial electromagnetic force to constrain the actual geometric center position of AMB to track the resting geometric center position, ensuring that the 5-DOF constraint of the payload relative to the platform except for axial rotation holds. As an alternative, the TB works when the AMB fails, avoiding structural damage and mission failure.

The coordinate frames and position vectors used in this section are shown in Figure 3.

Where o is the inertial coordinate frame, b is the platform's body-fixed coordinate frame, and p is the payload's body-fixed coordinate frame. $wi(i = x, y, z)$ is the momentum wheel i body-fixed coordinate frame (Figure 3 takes the momentum wheel x as an example), wt is the body-fixed coordinate frame of momentum wheel t installed in the payload, and $ak(k = 1, 2)$ is the solar panel k body-fixed coordinate frame (Figure 3 takes the solar panel 1 as an example).

Where X_c, X_{pf}, and X_{pl} are the position vectors of the RPS system's centroid, the platform subsystem's centroid, and the payload subsystem's centroid, respectively. r_s is the position vector from the platform subsystem's centroid to the coordinate origin of b. r_{ak} is the position vector from the platform subsystem's centroid to the solar panel k installation position. ρ_k and ρ_{ck} are the position vectors from the
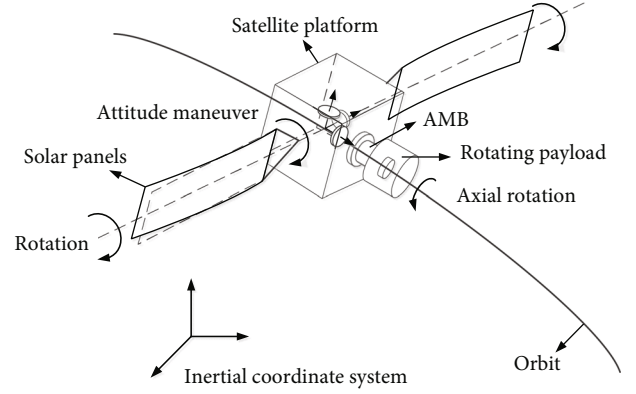

FIGURE 1: Structure of the RPS system.

installation position to a certain mass point dm and the centroid of solar panel k, respectively. r_P is the position vector from the RPS system's centroid to the coordinate origin of p. r_k is the position vector from the coordinate origin of p to the payload subsystem's centroid. r_l is the position vector from the coordinate origin of b to the coordinate origin of p.

Notation: for a given vector projection $r = [r_1, r_2, r_3]^T \in R^3$, we use $\tilde{r} \in R^{3 \times 3}$ to denote the cross-product antisymmetric matrix operation. $\|r\|$ is the Euclidean norm, diag $(r) \in R^{3 \times 3}$ is the diagonal matrix with r as the diagonal element, $\dot{r} \in R^3$ is the time derivative, and $\ddot{r}$ is the second time derivative. sgn $(r) = [\text{sgn} (r_1), \text{sgn} (r_2), \text{sgn} (r_3)]^T \in R^3$ and $\text{sig}^a(r) = [|r_1|^a \text{ sgn} (r_1), |r_2|^a \text{ sgn} (r_2), |r_3|^a \text{ sgn} (r_3)]^T \in R^3$, where $a \in \mathbb{R}$ and sgn $(.)$ denote the sign function.

2.1. Dynamic Model of RPS. The dynamic model of the platform subsystem is given as follows.

$$M_{pf}\ddot{X}_{pf} + \sum_{k=1,2} P_{ak}D_{ak}\ddot{\theta}_{ak} + \sum_{k=1,2} \gamma_{tk}\ddot{\eta}_k = -A_b F_{mb},$$

$$J_{pf}\dot{\omega}_{pf} + \dot{J}_{pf}\omega_{pf} + \sum_{i=x,y,z} R_{wi}D_{wi}\ddot{\theta}_{wi}$$

$$+ \sum_{k=1,2} \left(R_{ak}D_{ak}\ddot{\theta}_{ak} + \gamma_{sk}\ddot{\eta}_k \right)$$

$$+ \tilde{\omega}_{pf} \left(J_{pf}\omega_{pf} + \sum_{i=x,y,z} R_{wi}D_{wi}\dot{\theta}_{wi} \right.$$

$$\left. + \sum_{k=1,2} \left(R_{ak}D_{ak}\dot{\theta}_{ak} + \gamma_{sk}\dot{\eta}_k \right) \right) = \tau_b,$$

$$J_{Wi}\ddot{\theta}_{wi} + \dot{\omega}_{pf}{}^T R_{wi}D_{wi} = \tau_{wi}(i = x, y, z),$$

$$J_{Ak}\ddot{\theta}_{ak} + \ddot{X}_{pf}{}^T P_{ak}D_{ak} + \dot{\omega}_{pf}{}^T R_{ak}D_{ak}$$

$$+ D_{ak}{}^T \gamma_{ak}\ddot{\eta}_k = \tau_{ak}(k = 1, 2),$$

$$\ddot{\eta}_k + \gamma_{tk}{}^T \ddot{X}_{pf} + \gamma_{sk}{}^T \dot{\omega}_{pf} + \gamma_{ak}{}^T D_{ak}\ddot{\theta}_{ak}$$

$$+ \Omega_k{}^2 \eta_k + 2\zeta_k \Omega_k \dot{\eta}_k = 0(k = 1, 2).$$
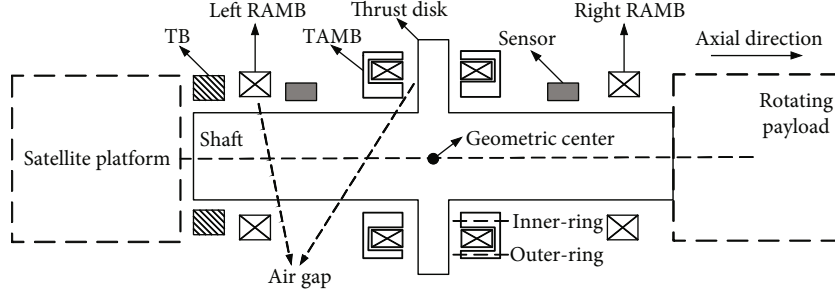
$$(1)$$

FIGURE 2: Structure of the AMB subsystem.
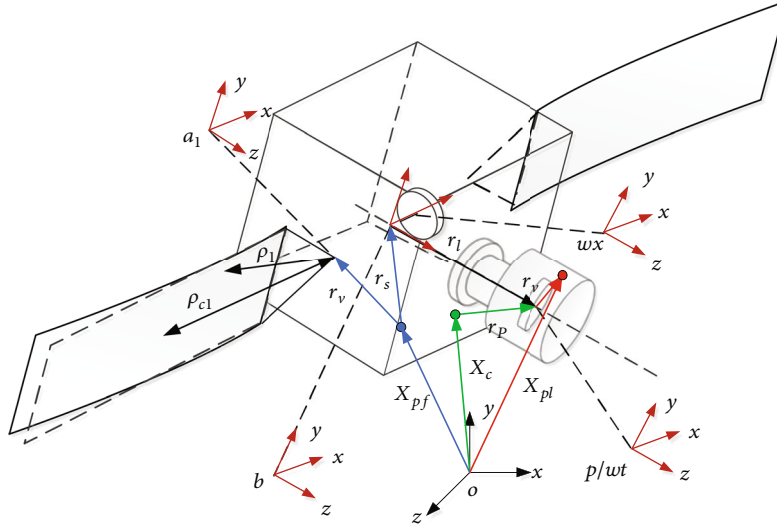

FIGURE 3: Coordinate frames and vectors used for modeling.

And the dynamic model of the payload subsystem is given as follows.

$$M_{pl}\ddot{X}_{pl} = A_b F_{mb},$$

$$J_{pl}\dot{\omega}_{pl} + R_{wt}D_{wt}\ddot{\theta}_{wt} + \tilde{\omega}_{pl}\left(J_{pl}\omega_{pl} + R_{wt}D_{wt}\dot{\theta}_{wt}\right) = \tau_p, \quad (2)$$

$$J_{Wt}\ddot{\theta}_{wt} + \dot{\omega}_{pl}^T R_{wt}D_{wt} = \tau_{wt},$$

where X_{pf} and X_{pl} are the projections of $\textbf{\textit{X}}_{pf}$ and $\textbf{\textit{X}}_{pl}$ in o, respectively. M_{pf} and J_{pf} are the mass and inertia matrix of the platform subsystem, while M_{pl} and J_{pl} are the definitions of the payload subsystem. ω_{pf} and ω_{pl} denote the angular velocity vector projection of the satellite platform and the rotating payload under their body-fixed coordinate frame, respectively. θ_{wi}, R_{wi}, and J_{wi} denote the rotation angle relative to the satellite platform, rotation coupling matrix with the satellite platform attitude, and inertia matrix of the momentum wheel i, respectively. In addition, J_{Wi} is the i-axis principal inertia of J_{wi}, and D_{wi} is the projection matrix of the relative angular velocity vector of momentum wheel i under its body-fixed reference frame, such as $D_{wx} = [1, 0, 0]^T$. Similarly, θ_{wt}, R_{wt}, J_{wt}, J_{Wt}, and D_{wt} are the definitions of

momentum wheel t. Furthermore, θ_{ak}, R_{ak}, J_{ak}, J_{Ak}, and D_{ak} are the definitions of the solar panel k, and P_{ak} is the translation coupling matrix with the satellite platform. Solar panel vibration is described by mode coordinate η_k and mode frequency matrix Ω_k. γ_{ak}, γ_{tk}, and γ_{sk} denote the coupling matrix between the solar panel vibration and θ_{ak}, X_{pf}, and ω_{pf}, respectively. τ_{wi} and τ_{wt} denote the driving torques of the momentum wheel i and t, respectively. A_b is the attitude matrix of b relative to o. To give a more thorough description of Equation (1), the expressions of the coupling matrixes mentioned above are as follows.

$$P_{ak} = A_b A_k M_k \tilde{\rho}_{ck}^T, \gamma_{tk} = A_b A_k \int_k \Phi_k dm,$$

$$R_{ak} = \tilde{r}_{ak} A_k M_k \tilde{\rho}_{ck}^T + A_k J_{ak}, \gamma_{ak} = \int_k \tilde{\rho}_k \Phi_k dm, \gamma_{sk} \quad (3)$$

$$= \tilde{r}_{ak} A_k \int_k \Phi_k dm + A_k \int_k \tilde{\rho}_k \Phi_k dm,$$

where r_{ak} is the projection of $\textbf{\textit{r}}_{ak}$ in b, ρ_k and ρ_{ck} are the projections of $\boldsymbol{\rho}_k$ and $\boldsymbol{\rho}_{ck}$ in ak, A_k is the attitude matrix of ak relative to b, and M_k and Φ_k are the mass and mode shape function of solar panel k, respectively.

Defining F_{mb} and τ_{mb} as the resultant force projection and torque projection of AMB acting on payload in b, respectively, which can be expressed as follows.

$$\begin{cases} F_{mb} = Kr_{5b} + C\dot{r}_{5b}, \\ \tau_{mb} = K_a \vartheta + C_a \dot{\vartheta}, \end{cases} \quad (4)$$

where $K \in R^{3\times3}$, $K_a \in R^{3\times3}$, $C \in R^{3\times3}$, and $C_a \in R^{3\times3}$ are the bearing mechanical characteristics parameters, specifically, K and K_a are the displacement stiffness matrix and angular stiffness matrix of the AMB, respectively, and C and C_a are the displacement damping matrix and angular damping matrix of the AMB, respectively. r_{5b} is the projection of the vector from the AMB's resting geometric center position to the AMB's actual geometric center position in b, i.e., the position deviation of the AMB. $\vartheta = [\varphi, \theta, \psi]^T$ is the Euler angle of the payload relative to the satellite platform, i.e., the angular deviation of the AMB. Based on Equation (4), τ_b and τ_p can be expressed as follows.

$$\tau_b = -\tilde{r}_{fb}(Kr_{5b} + C\dot{r}_{5b}) - K_a\vartheta - C_a\dot{\vartheta}, \quad (5)$$

$$\tau_p = \tilde{r}_{gp}(A_b^p)^T(Kr_{5b} + C\dot{r}_{5b}) + (A_b^p)^T(K_a\vartheta + C_a\dot{\vartheta}), \quad (6)$$

where r_{fb} is the projection of the vector from platform subsystem's centroid to the AMB's actual geometric center position in b, r_{gp} is the projection of the vector from payload subsystem's centroid to the AMB's actual geometric center position in p, and A_b^p is the attitude matrix of p relative to b. Combining with Equations (1)–(6), the refined dynamic model of the RPS system has been established, and more details about Equations (1)–(6) can be found in [7].

2.2. Dynamic Model of Lumped Disturbance. Note that the models established in the previous subsection are applicable to any phase. In the imaging phase, the inertial force in F_{mb} and the inertial torque in τ_{mb} are small, i.e., the lumped torque τ_b transmitted from the AMB to the satellite platform, denoted as the lumped disturbance d, is mainly composed of dynamic unbalanced disturbance and static unbalanced disturbance. In this section, the dynamic model of the lumped disturbance d is proposed. Before modeling, the following assumptions are made to simplify the analysis.

Assumption 1. The radial angle deviation and displacement deviation of AMB can be omitted, i.e., the following equations approximately.

$$\vartheta = [0, 0, \psi]^T, \dot{\vartheta} = [0, 0, \dot{\psi}]^T, r_{5b} = \dot{r}_{5b} = 0^{3\times1}. \quad (7)$$

Assumption 2. The system states are stable, $\dot{\omega}_{pf} = \ddot{\vartheta} = 0^{3\times1}$ hold. The orbital angular velocity is denoted as ω_0, and the desired rotational speed of payload is $\dot{\psi}_d$. Assuming that the state tracking errors are small, i.e., the following equations approximately.

$$\omega_{pf} = [\omega_0, 0, 0]^T, \dot{\psi} = \dot{\psi}_d. \quad (8)$$

As shown in Figure 3, the centroid of momentum wheel t and the coordinate origin of p are coincident. Define r_k to be the projection of $\boldsymbol{r}_k$ in p, $r_j = [r_{jx}, r_{jy}, r_{jz}]^T$ to be the projection of the vector from coordinate origin of p to payload's centroid in p (i.e., static unbalance) and M_p to be the payload's mass, then $r_k = M_p r_j / M_{pl}$ holds. On this basis, the following equation can be obtained.

$$M_{pl}X_{pl} = M_{pl}(X_p + A_p r_k) = M_{pl}\left(X_c + A_b r_P + A_p \frac{M_p}{M_{pl}} r_j\right)$$
$$= M_p(X_c + A_b r_P + A_p r_j) + M_{wt}(X_c + A_b r_P), \quad (9)$$

where X_c is the projection of $\boldsymbol{X_c}$ in o, X_p is the position vector projection of the coordinate origin of p in o, A_p is the attitude matrix of p relative to o, M_{wt} is the mass of momentum wheel t, and $M_{pl} = M_p + M_{wt}$ holds. $r_P = [r_{Px}, r_{Py}, r_{Pz}]^T$ is the projection of $\boldsymbol{r_P}$ in b, which can be expressed as follows.

$$r_P = \sigma(r_s + r_l) - \varepsilon A_b^p r_j, \quad (10)$$

where $r_s = [r_{sx}, r_{sy}, r_{sz}]^T$ is the projection of $\boldsymbol{r_s}$ in b, r_l is the projection of $\boldsymbol{r_l}$ in b, and $\sigma = (M_{pf} + M_{pl})^{-1}M_{pf}$ and $\varepsilon = (M_{pf} + M_{pl})^{-1}M_p$ hold.

Combining Equations (2) and (9), one has

$$F_{mb} = M_{pl}\left(A_b{}^T\ddot{X}_c + \tilde{\omega}_{pf}\tilde{\omega}_{pf}r_P + \dot{\tilde{\omega}}_{pf}r_P + 2\tilde{\omega}_{pf}\dot{r}_P + \ddot{r}_P\right)$$
$$+ M_p\left(A_b^p\tilde{\omega}_{pl}\tilde{\omega}_{pl}r_j + A_b^p\dot{\tilde{\omega}}_{pl}r_j\right). \quad (11)$$

When Assumption 1 holds, it follows that

$$A_b^p = \begin{bmatrix} \cos\psi & -\sin\psi & 0 \\ \sin\psi & \cos\psi & 0 \\ 0 & 0 & 1 \end{bmatrix}, \omega_{lf} = \dot{\vartheta}, \dot{r}_P$$
$$= -\varepsilon A_b^p\tilde{\omega}_{lf}r_j, \ddot{r}_P = -\varepsilon A_b^p\tilde{\omega}_{lf}\tilde{\omega}_{lf}r_j - \varepsilon A_b^p\dot{\tilde{\omega}}_{lf}r_j, \quad (12)$$

where ω_{lf} is the projection of the angular velocity of the payload relative to the satellite platform in p. Furthermore, when Assumption 2 holds, it follows that

$$\omega_{pl} = \begin{bmatrix} \omega_0 \cos \psi_d \\ -\omega_0 \sin \psi_d \\ \dot{\psi}_d \end{bmatrix}, \dot{\omega}_{pl} = -\begin{bmatrix} \dot{\psi}_d \omega_0 \sin \psi_d \\ \dot{\psi}_d \omega_0 \cos \psi_d \\ 0 \end{bmatrix},$$

$$\dot{r}_P = -\varepsilon \dot{\psi}_d \begin{bmatrix} -r_{jy} \cos \psi_d - r_{jx} \sin \psi_d \\ -r_{jy} \sin \psi_d + r_{jx} \cos \psi_d \\ 0 \end{bmatrix}, \tag{13}$$

$$\ddot{r}_P = -\varepsilon \dot{\psi}_d{}^2 \begin{bmatrix} -r_{jx} \cos \psi_d + r_{jy} \sin \psi_d \\ -r_{jx} \sin \psi_d - r_{jy} \cos \psi_d \\ 0 \end{bmatrix}.$$

Bringing Equations (12) and (13) into Equation (11) and noting $F_{mb} = [F_{mb,x}, F_{mb,y}, F_{mb,z}]^T$, one has

$$F_{mb,x} = (M_{pl}\varepsilon - M_p)\dot{\psi}_d{}^2(r_{jx}\cos \psi_d - r_{jy}\sin \psi_d),$$

$$F_{mb,y} = (M_{pl}\varepsilon - M_p)\dot{\psi}_d{}^2(r_{jx}\sin \psi_d + r_{jy}\cos \psi_d) - M_{pl}\omega_0^2 r_{Py},$$

$$F_{mb,z} = (2M_p - 2M_{pl}\varepsilon)\omega_0\dot{\psi}_d(r_{jx}\cos \psi_d - r_{jy}\sin \psi_d)$$
$$- M_p(r_{jz} + r_{Pz})\omega_0^2 - \omega_0^2 r_{Pz}M_{wt}. \tag{14}$$

For the convenience of subsequent modeling, F_{mb} is divided into F_{mb1} and F_{mb2}, where $F_{mb1} = [F_{mb1,x}, F_{mb1,y}, F_{mb1,z}]^T$ is the resultant force on the payload, and $F_{mb2} = [F_{mb2,x}, F_{mb2,y}, F_{mb2,z}]^T$ is the resultant force on the momentum wheel t, one has

$$F_{mb1,x} = M_p(\varepsilon - 1)\dot{\psi}_d{}^2(r_{jx}\cos \psi_d - r_{jy}\sin \psi_d),$$

$$F_{mb1,y} = M_p(\varepsilon - 1)\dot{\psi}_d{}^2(r_{jx}\sin \psi_d + r_{jy}\cos \psi_d) - M_p\omega_0^2 r_{Py},$$

$$F_{mb1,z} = 2M_p(1 - \varepsilon)\omega_0\dot{\psi}_d(r_{jx}\cos \psi_d - r_{jy}\sin \psi_d)$$
$$- M_p(r_{jz} + r_{Pz})\omega_0^2, \tag{15}$$

$$F_{mb2,x} = M_{wt}\varepsilon\dot{\psi}_d{}^2(r_{jx}\cos \psi_d - r_{jy}\sin \psi_d),$$

$$F_{mb2,y} = M_{wt}\varepsilon\dot{\psi}_d{}^2(r_{jx}\sin \psi_d + r_{jy}\cos \psi_d) - M_{wt}\omega_0^2 r_{Py},$$

$$F_{mb2,z} = -2M_{wt}\varepsilon\omega_0\dot{\psi}_d(r_{jx}\cos \psi_d - r_{jy}\sin \psi_d) - M_{wt}\omega_0^2 r_{Pz}. \tag{16}$$

Dividing r_P into r_{P1} and $r_{P2} = [r_{P2,x}, r_{P2,y}, r_{P2,z}]^T$, where r_{P1} is the projection of the vector from RPS system's centroid to AMB's actual geometric center position in b, and $r_{P2} = r_P - r_{P1}$ holds. Then, based on Equations (2) and (5), the following equation can be obtained.

$$\tau_{mb} = A_b^p J_{pl}\dot{\omega}_{pl} + A_b^p R_{wt} D_{wt}\ddot{\theta}_{wt}$$
$$+ A_b^p \tilde{\omega}_{pl}\left(J_{pl}\omega_{pl} + R_{wt} D_{wt}\dot{\theta}_{wt}\right)$$
$$+ \left(\tilde{r}_{P2} + \frac{M_p}{M_{pl}} A_b^p \tilde{r}_j (A_b^p)^T\right) F_{mb}. \tag{17}$$

The inertia matrix of the rotating payload is denoted as J_p and consists of the principal inertia I_x, I_y, and I_z and the inertia product I_{xy}, I_{xz}, and I_{yz} (i.e., dynamic unbalance). The following equation holds.

$$J_{pl} = J_p + \frac{M_p}{M_{pl}} M_{wt}\tilde{r}_j\tilde{r}_j{}^T + J_{wt}. \tag{18}$$

Bringing Equation (18) into Equation (17), when Assumption 1 and Assumption 2 hold, $\tau_{mb} = [\tau_{mb,x}, \tau_{mb,y}, \tau_{mb,z}]^T$ can be given as

$$\tau_{mb,x} = -(I_x - I_y)\dot{\psi}_d\omega_0 \sin 2\psi_d + 2I_{xy}\dot{\psi}_d\omega_0 \cos 2\psi_d$$
$$+ \dot{\psi}_d{}^2(I_{xz}\sin \psi_d + I_{yz}\cos \psi_d)$$
$$- (r_{P2,z} + r_{jz})F_{mb1,y} + (r_{jy}\cos \psi_d$$
$$+ r_{jx}\sin \psi_d)F_{mb1,z} - r_{P2,z}F_{mb2,y},$$

$$\tau_{mb,y} = \omega_0\dot{\psi}_d(I_x - I_y)\cos 2\psi_d + 2\dot{\psi}_d\omega_0 I_{xy}\sin 2\psi_d$$
$$+ \dot{\psi}_d{}^2(I_{yz}\sin \psi_d - I_{xz}\cos \psi_d)$$
$$- \omega_0\left[I_z\dot{\psi}_d + J_{wtz}\left(\dot{\psi}_d + \dot{\theta}_{wt}\right)\right]$$
$$+ (r_{P2,z} + r_{jz})F_{mb1,x} + (r_{jy}\sin \psi_d$$
$$- r_{jx}\cos \psi_d)F_{mb1,z} + r_{P2,z}F_{mb2,x}, \tag{19}$$

$$\tau_{mb,z} = \frac{1}{2}(I_x - I_y)\omega_0{}^2 \sin 2\psi_d - I_{xy}\omega_0{}^2 \cos 2\psi_d$$
$$- (r_{jy}\cos \psi_d + r_{jx}\sin \psi_d)F_{mb1,x}$$
$$+ (-r_{jy}\sin \psi_d + r_{jx}\cos \psi_d)F_{mb1,y}.$$

According to the definitions of r_{fb}, r_s, r_l, and r_{P2}, it is clear that $r_{fb} = r_s + r_l - r_{p2}$ holds. Furthermore, based on Equations (5), (15), (16), and (19), the lumped disturbance $d = [d_x, d_y, d_z]^T$ transmitted by the AMB, consisting of inertia difference disturbance d_1, axial angular momentum disturbance d_2, dynamic unbalanced disturbance d_3, and static unbalanced disturbance d_4, can be modeled as

$$d_1 = \begin{bmatrix} (I_x - I_y)\dot{\psi}_d\omega_0 \sin 2\psi_d \\ -\omega_0\dot{\psi}_d(I_x - I_y)\cos 2\psi_d \\ \dfrac{-(I_x - I_y)\omega_0{}^2(\sin 2\psi_d)}{2} \end{bmatrix},$$

$$d_2 = \begin{bmatrix} 0 \\ \omega_0 I_z\dot{\psi}_d + \omega_0 J_{wtz}\left(\dot{\psi}_d + \dot{\theta}_{wt}\right) \\ 0 \end{bmatrix},$$

$$d_3 = \begin{bmatrix} -2I_{xy}\dot{\psi}_d\omega_0 \cos 2\psi_d - \dot{\psi}_d^2 (I_{xz} \sin \psi_d + I_{yz} \cos \psi_d) \\ -2\dot{\psi}_d\omega_0 I_{xy} \sin 2\psi_d - \dot{\psi}_d^2 (I_{yz} \sin \psi_d - I_{xz} \cos \psi_d) \\ I_{xy}\omega_0^2 \cos 2\psi_d \end{bmatrix},$$

(20)

$$d_{4x} = (r_{sz} + r_{lz} + r_{jz})F_{mb1,y}$$
$$- (r_{sy} + r_{jy} \cos \psi_d + r_{jx} \sin \psi_d)F_{mb1,z}$$
$$+ (r_{sz} + r_{lz})F_{mb2,y} - r_{sy}F_{mb2,z},$$

$$d_{4y} = -(r_{sz} + r_{lz} + r_{jz})F_{mb1,x}$$
$$+ (r_{sx} + r_{jx} \cos \psi_d - r_{jy} \sin \psi_d)F_{mb1,z}$$
$$- (r_{sz} + r_{lz})F_{mb2,x} + r_{sx}F_{mb2,z},$$

$$d_{4z} = (r_{sy} + r_{jy} \cos \psi_d + r_{jx} \sin \psi_d)F_{mb1,x}$$
$$- (r_{sx} - r_{jy} \sin \psi_d + r_{jx} \cos \psi_d)F_{mb1,y}$$
$$+ r_{sy}F_{mb2,x} - r_{sx}F_{mb2,y}.$$

(21)

TABLE 1: Payload inertia parameter values for different cases.

	Principal inertia $(kg \cdot m^2)$	Dynamic unbalance $(kg \cdot m^2)$	Static unbalance (mm)
Case 1	$I_x = 114.4$ $I_y = 311.8$ $I_z = 252.9$	$I_{xz} = 1$ $I_{xy} = I_{yz} = 0$	$x = 1, y = 0,$ $z = -9.6$
Case 2	$I_x = 214.4$ $I_y = 211.8$ $I_z = 252.9$	$I_{xz} = 3.9$ $I_{xy} = I_{yz} = 0$	$x = 5, y = 0,$ $z = -9.6$
Case 3	$I_x = 214.4$ $I_y = 211.8$ $I_z = 252.9$	$I_{xz} = 6.9$ $I_{xy} = I_{yz} = 0$	$x = 7, y = 0,$ $z = -9.6$

TABLE 2: Theoretical results of case 1.

	d_1	d_2	d_3	d_4
Amplitude (Nm)	0.061	0.008	0.078	0.099
Frequency (Hz)	0.088	/	0.044	0.044

2.3. Disturbance Analysis. Equations (20) and (21) provide mechanical constraints on the payload mass parameters such as the radial principal inertia, dynamic unbalance, and static unbalance. Based on these two equations, the feasibility of the current balancing error index can be judged. To illustrate this point, the maximum torque of the satellite platform momentum wheel is 1 Nm, $\omega_0 = 0.0011$ rad/s, $\dot{\psi}_d$ = 16 deg/s, and the compensation accuracy of axial angular momentum disturbance is 10%, three balancing errors are considered: $1 kg \cdot m^2$ and 1mm, $3.9 kg \cdot m^2$ and 5mm, and $6.9 kg \cdot m^2$ and 7mm. The real dynamic unbalance and static unbalance are taken randomly within the respective error boundary, where the cases that make the lumped disturbance take their respective maximum values, denoted as cases 1-3, as shown in Table 1.

The theoretical results of d_1-d_4 for case 1 are summarized in Table 2. From case 1, it can be concluded that the inertia difference of payload does not lead to excessive disturbance even if it increases to $197.4 kgm^2$, and the axial angular momentum disturbance d_2 is small constant. Therefore, when the dynamic unbalance and static unbalance increase, the lumped disturbance is mainly composed of d_3 and d_4.

The theoretical results of the lumped disturbance in the three cases are shown in Figure 4. In case 2, the lumped disturbance increases significantly when the unbalance increases. Furthermore, there is a risk that the lumped disturbance may exceed the maximum torque of the momentum wheel, as shown in case 3, and the control law cannot adjust the excess part, which will inevitably affect the attitude accuracy and stability of the satellite system. Therefore, more attention should be paid to the payload balancing error index. Under the condition of the maximum torque of 1 Nm, case 2 has a certain margin, which is a reasonable scheme. Similarly, using Equations (20) and (21), the actuator can be selected according to the balancing error index, e.g., in

case 3, a momentum wheel with a maximum torque of 1.5 Nm needs to be selected instead of 1 Nm.

It should be noted that Equations (20) and (21) are established on the basis that Assumptions 1 and 2 hold. In practice, when the stiffness and damping of AMB is low, the radial angle deviation and displacement deviation of AMB cannot be omitted, i.e., Assumption 1 does not hold, which is manifested as the lumped disturbance d will be amplified in transfer process. Similarly, when the control accuracy of the satellite platform is low, i.e., Assumption 2 does not hold, the lumped disturbance d will also be amplified because of the inertial part. However, even if the two assumptions are violated, Equations (20) and (21) have sufficient accuracy, and the related simulation results will be given in Section 4.

3. Controller Design

3.1. Control System Model. To simplify the analysis, the solar panel is considered as a rigid body, and its rotation relative to the satellite platform is ignored. Then, Equation (1) can be simplified as

$$M_{pf}\ddot{X}_{pf} = -A_b F_{mb},$$

$$J_{pf}\dot{\omega}_{pf} + \sum_{i=x,y,z} R_{wi}D_{wi}\ddot{\theta}_{wi} + \tilde{\omega}_{pf}\left(J_{pf}\omega_{pf}\right.$$

$$\left. + \sum_{i=x,y,z} R_{wi}D_{wi}\dot{\theta}_{wi}\right) = \tau_b,$$

$$J_{Wi}\ddot{\theta}_{wi} + \dot{\omega}_{pf}^T R_{wi}D_{wi} = \tau_{wi}(i = x, y, z).$$

(22)

Furthermore, simplifying the driving equations of the momentum wheels i, and assuming that the flywheels are all installed in the forward direction. Note that $u = -[\tau_{wx}, \tau_{wy}, \tau_{wz}]^T$ is the control torque, one has

$$J_{pfn}\dot{\omega}_{pf} + \tilde{\omega}_{pf}J_{pfn}\omega_{pf} + \tilde{\omega}_{pf}\sum_{i=x,y,z} R_{wi}D_{wi}\dot{\theta}_{wi} = u + d', \quad (23)$$

where J_{pfn} denotes the nominal value of J_{pf}, $\Delta J_{pf} = J_{pf} - J_{pfn}$ denotes the parameter uncertainty, and $d' = d - \Delta J_{pf}\dot{\omega}_{pf} - \tilde{\omega}_{pf}\Delta J_{pf}\omega_{pf}$ holds. Define the quaternion of the satellite platform as $q_{pf} = [q_{pf,0}, q_{pf,b}^T]^T$, where $q_{pf,0}$ and $q_{pf,b} \in R^3$ are the scalar and vector components of the quaternion q_{pf}, respectively, satisfying $q_{pf,0}^2 + q_{pf,b}^T q_{pf,b} = 1$. In addition, if the desired quaternion of the satellite platform is $q_d = [q_{d0}, q_{db}^T]^T$, the error quaternion $q_e = [q_{e0}, q_{eb}^T]^T$ is obtained as follows:

$$q_{e0} = q_{db}^T q_{pf,b} + q_{d0}q_{pf,0}, q_{eb} = q_{d0}q_{pf,b} - \tilde{q}_{db}q_{pf,b} - q_{pf,0}q_{db}. \quad (24)$$

Furthermore, defining the attitude error matrix as $A(q_e)$ and the desired angular velocity as ω_d, then, the error angular velocity ω_e can be expressed as $\omega_e = \omega_{pf} - \omega_r$, where $\omega_r = A(q_e)^T\omega_d$. Therefore, Equation (23) can be expressed as

$$\dot{\omega}_e = -\dot{\omega}_r - J_{pfn}^{-1}\tilde{\omega}_{pf}J_{pfn}\omega_{pf} - J_{pfn}^{-1}\tilde{\omega}_{pf}\sum_{i=x,y,z} R_{wi}D_{wi}\dot{\theta}_{wi}$$
$$+ J_{pfn}^{-1}u + J_{pfn}^{-1}d'. \quad (25)$$

And the error quaternion attitude kinematics equations are

$$\dot{q}_{e0} = -\frac{1}{2}\omega_e^T q_{eb}, \dot{q}_{eb} = Q(q_e)\omega_e, \quad (26)$$

where $Q(q_e) = (\tilde{q}_{eb} + q_{e0}I_3)/2$ holds. On the basis of $\dot{Q}(q_e)\omega_e = -q_{eb}\omega_e^T\omega_e/4$ [21] holds, combining Equations (25) and (26), one has

$$\ddot{q}_{eb} = h + Bu + D, \quad (27)$$

where $B = Q(q_e)J_{pfn}^{-1}$, $D = Bd'$, and h satisfies

$$h = -\frac{1}{4}q_{eb}\omega_e^T\omega_e + Q(q_e)\left(-\dot{\omega}_r - J_{pfn}^{-1}\tilde{\omega}_{pf}J_{pfn}\omega_{pf}\right.$$
$$\left. - J_{pfn}^{-1}\tilde{\omega}_{pf}\sum_{i=x,y,z} R_{wi}D_{wi}\dot{\theta}_{wi}\right). \quad (28)$$

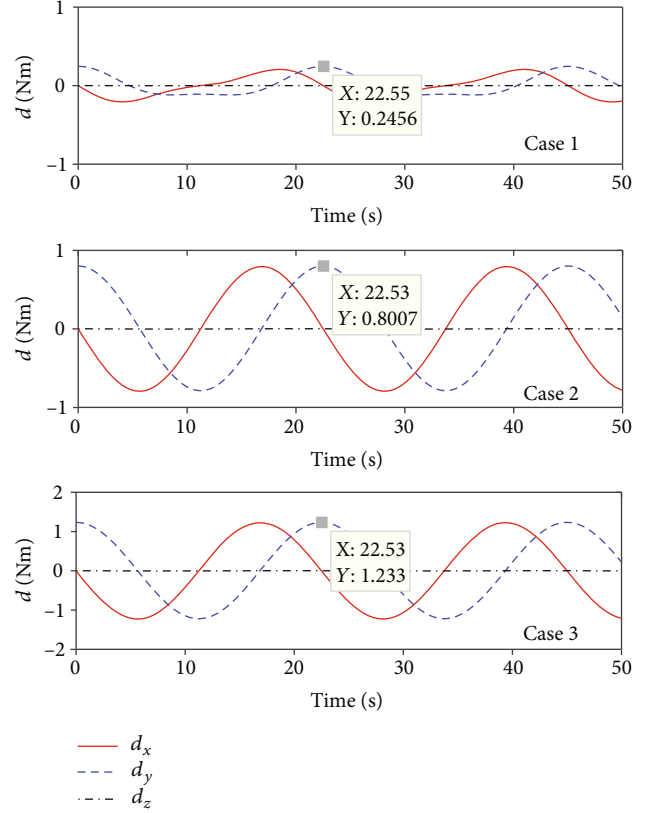Up to now, the dynamic model for controller design

Figure 4: Theoretical results of the lumped disturbance.

has been established. In this paper, the control objective is to design the controller u, such that the states q_{pf} and ω_{pf} can follow the desired states q_d and ω_d in a fixed time in spite of unknown lumped disturbance and uncertainty, i.e., there exist a constant $T_{max} > 0$ such that $q_{eb} = 0^{3\times1}$ and $\omega_e = 0^{3\times1}$ hold for all $t > T_{max}$.

3.2. Definition and Lemmas. Before the controller design, some useful definitions and theorems need to be provided.

Consider the following nonlinear system:

$$\dot{x} = f(x(t)), x(0) = x_0, f(0) = 0, \quad (29)$$

where $x \in R^n$ and $f : R^n \longrightarrow R^n$ are a nonlinear function.

Definition 3 (see [35]). The system (29) is called finite-time convergent to the origin for an initial condition x_0, if it is Lyapunov stable and there exists a settling time function $T(x_0)$ such that the system state $x(t, x_0) \in R^n$ is equal to zero, for all $t \geq T(x_0)$.

Definition 4 (see [36]). The system (29) is called fixed-time convergent to the origin, if the origin is globally finite-time stable and the settling time function $T(x_0)$ is bounded by positive constant $T_{max} > 0$, i.e., the system state $x(t, x_0) \in R^n$ is equal to zero, for all $t \geq T_{max}$, starting from any initial condition x_0.

Lemma 5 (see [29]). *For system (29), suppose there exists a Lyapunov function $V(x)$, scalars α_1, β_1, p, q, $k \in R^+$, $pk < 1$, and $qk > 1$, such that $\dot{V}(x) \leq -(\alpha_1 V(x)^p + \beta_1 V(x)^q)^k$. Then, the system is fixed-time stable. Furthermore, the upper bound of the convergence time is given as follows.*

$$T \leq \frac{1}{\alpha_1^k(1-pk)} + \frac{1}{\beta_1^k(qk-1)}. \tag{30}$$

Lemma 6 (see [27]). *For $x_i \in \mathbb{R}$, $i = 1, 2, \cdots, n$, $0 < \chi_1 \leq 1$, and $\chi_2 > 1$, the following inequalities hold:*

$$\left(\sum_{i=1}^{n}|x_i|\right)^{\chi_1} \leq \sum_{i=1}^{n}|x_i|^{\chi_1}, \left(\sum_{i=1}^{n}|x_i|\right)^{\chi_2} \leq n^{\chi_2-1}\sum_{i=1}^{n}|x_i|^{\chi_2}. \tag{31}$$

Assumption 7. The unknown disturbance D is bounded and continuously differentiable with respect to time, such that satisfy $\|D\| \leq D_m$ and $\|\dot{D}\| \leq L$, where D_m and L are a positive constant.

Assumption 8. System states q_{eb} and $\dot{q}_{eb}$ in dynamic model (27) can be both measured.

3.3. Fixed-Time Extended State Observer. To estimate the unknown disturbance D in dynamic model (27), define $x_1 = \dot{q}_{eb}$, and the extended state $x_2 = D$, the fixed-time extended state observer equation is designed as follows:

$$\dot{Z}_1 = Z_2 - \lambda_1\frac{e_1}{\|e_1\|^{1/2}} - \lambda_2 e_1\|e_1\|^{\zeta-1} + h + Bu, \dot{Z}_2 = -\lambda_3\frac{e_1}{\|e_1\|}, \tag{32}$$

where $Z_1 \in R^3$, $Z_2 \in R^3$, $\lambda_3 > 4L$, $\lambda_1 > \sqrt{2\lambda_3}$, $\lambda_2 > 0$, and $\zeta > 1$. Then, the observer error $e_1 = Z_1 - x_1$ and $e_2 = Z_2 - x_2$ can be expressed as

$$\dot{e}_1 = -\lambda_1\frac{e_1}{\|e_1\|^{1/2}} - \lambda_2 e_1\|e_1\|^{\zeta-1} + e_2, \dot{e}_2 = -\lambda_3\frac{e_1}{\|e_1\|} - \dot{D}. \tag{33}$$

According to the theorem proposed in [36], both states $e_1(t)$ and $e_2(t)$ converge to the origin uniformly in fixed time T_o, where T_o satisfies

$$T_o \leq \left(\frac{1}{\lambda_2(\zeta-1)\eta^{\zeta-1}} + \frac{2\left(\sqrt{3}\eta\right)^{1/2}}{\lambda_1} + \frac{K}{M}\right)$$
$$\times \left(1 + \frac{M}{m\left(1 - \sqrt{2\lambda_3/\lambda_1}\right)}\right) + \frac{\sqrt{3}K}{m}, \tag{34}$$

where $M = \lambda_3 + L$, $m = \lambda_3 - L$, $\eta = \left(3^{1/4}\lambda_1/\lambda_2\right)^{1/(\zeta+0.5)}$, and $K \geq \|e_2(0)\|$. In this paper, since the initial value of Z_2 is taken as zero, so K can take D_m according to Assumption 7. More

information on the derivation of the upper bound for T_o can be found in [36].

Remark 9. It should be noted that the proposed FESO (32) is modified according to [36]. Compared with the fixed-time observers in [33, 34], observer (32) is much simpler for designing the observer parameters. Taking the observer in [33] as an example, a total of six parameters need to be designed in order to achieve unknown disturbance estimation, so this observer is much more difficult to be applied to space missions. However, the FESO (32) has only λ_1, λ_2, λ_3, and ζ to be designed, and it is clear that the proposed FESO achieves a more concise structure and fewer parameters to be designed. Therefore, in space missions, it is more convenient for the proposed FESO (32) to estimate the disturbance D within a fixed time.

3.4. Design of Controller

3.4.1. Fixed-Time Sliding Mode Surface. In this section, a novel QFNFTSMS is proposed:

$$s = K(q_{eb})q_{eb} + \text{sig}^{r_2}(\dot{q}_{eb}), \tag{35}$$

where $K(q_{eb})$ is a diagonal matrix, and the diagonal elements $k(q_{ebi})(i = 1, 2, 3)$ are denoted as

$$k(q_{ebi}) = \left(a|q_{ebi}|^{p-1/(kr_2)} + b|q_{ebi}|^{g-1/(kr_2)}\right)^{kr_2}, \tag{36}$$

where $a > 0$, $b > 0$, $k > 1$, $2 > r_2 > 1$, $1 < gk \leq 2k - 1$, and $1/r_2 < pk < 1$.

Theorem 10. *When $s = 0$ satisfies, q_{eb} and $\dot{q}_{eb}$ can converge to the origin uniformly within fixed time T_s in spite of the initial conditions. Meanwhile, q_{e0} and ω_e will converge to 1 (or -1) and $0^{3\times1}$, respectively: if $q_{e0}(0) > 0$, q_{e0} will converge to 1, if $q_{e0}(0) < 0$, q_{e0} will converge to -1. Where the upper bound of convergence time T_s satisfies*

$$T_s \leq \frac{2^{(1-pk)/2}}{a^k 3^{1-k}(1-pk)} + \frac{2^{(1-gk)/2}}{b^k 3^{1-k}(gk-1)}. \tag{37}$$

Proof. If $s = 0$ holds, that is, $\dot{q}_{eb} = -\text{sig}^{1/r_2}(K(q_{eb})q_{eb})$. Furthermore, we can obtain

$$\dot{q}_{ebi} = -\text{sig}^{1/r_2}(k(q_{ebi})q_{ebi})$$
$$= -\text{sig}^{1/r_2}\left[\left(a|q_{ebi}|^p + b|q_{ebi}|^g\right)^{kr_2}\text{sign}(q_{ebi})\right]$$
$$= -\left|a|q_{ebi}|^p + b|q_{ebi}|^g\right|^k\text{sign}(q_{ebi})$$
$$= -\text{sig}^k(a\text{sig}^p(q_{ebi}) + b\text{sig}^g(q_{ebi})). \tag{38}$$

□

Therefore, $\dot{q}_{eb} = -sig^k(asig^p(q_{eb}) + bsig^g(q_{eb}))$ holds, and $q_{eb} = 0^{3\times1}$ is the equilibrium point. Let the positive Lyapunov function be $V_1 = 0.5q_{eb}{}^T q_{eb}$, then, the derivative of V_1 is obtained as follows.

$$
\begin{aligned}
\dot{V}_1 &= -q_{eb}{}^T sig^k(asig^p(q_{eb}) + bsig^g(q_{eb})) \\
&= -\sum_{i=1}^{3} q_{ebi}|asig^p(q_{ebi}) + bsig^g(q_{ebi})|^k \operatorname{sign}(q_{ebi}) \\
&= -\sum_{i=1}^{3} \left| a\left(|q_{ebi}|^2\right)^{p+1/k/2} + b\left(|q_{ebi}|^2\right)^{g+1/k/2} \right|^k.
\end{aligned}
\tag{39}
$$

By Lemma 6, one has

$$
\begin{aligned}
\dot{V}_1 &\leq -3^{1-k}\left(\sum_{i=1}^{3} \left| a\left(|q_{ebi}|^2\right)^{p+1/k/2} + b\left(|q_{ebi}|^2\right)^{g+1/k/2} \right| \right)^k \\
&= -3^{1-k}\left(a\sum_{i=1}^{3}\left(|q_{ebi}|^2\right)^{p+1/k/2} + b\sum_{i=1}^{3}\left(|q_{ebi}|^2\right)^{g+1/k/2} \right)^k \\
&\leq -\left(3^{1-k/k}2^{p+1/k/2}aV^{p+1/k/2} + 3^{1-k/k}2^{p+1/k/2}bV^{g+1/k/2} \right)^k.
\end{aligned}
\tag{40}
$$

Then based on Lemma 5, q_{eb} can converge to the origin uniformly in bounded convergence time T_3 and T_3 satisfies Equation (37). Moreover, $\dot{q}_{eb}$ will converge to the origin, and ω_e will converge to the origin because of $\dot{q}_{eb} = Q(q_e)\omega_e$. However, whether q_{e0} will converge to 1 or -1 cannot be judged from V_1 and needs further discussion.

Note that when $s = 0$ satisfies, the following equation can be obtained based on Equation (26).

$$
\dot{q}_{e0} = \frac{q_{eb}{}^T sig^k(asig^p(q_{eb}) + bsig^g(q_{eb}))}{q_{e0}}.
\tag{41}
$$

If $q_{e0}(0) > 0$, then $\dot{q}_{e0} > 0$ holds at $t > 0$, so $q_{e0}(t) > 0$ holds for all $t > 0$; if $q_{e0}(0) < 0$, $\dot{q}_{e0} < 0$ holds at $t > 0$, so $q_{e0}(t) < 0$ holds for all $t > 0$. Furthermore, when $q_{e0}(0) > 0$, define $V_2 = q_{eb}{}^T q_{eb} + (1 - q_{e0})^2$, $V_3 = q_{eb}{}^T q_{eb} + (1 + q_{e0})^2$, the following inequalities hold.

$$
\begin{cases}
\dot{V}_2 = \dfrac{-2\sum_{i=1}^{3}\left| a\left(|q_{ebi}|^2\right)^{p+1/k/2} + b\left(|q_{ebi}|^2\right)^{g+1/k/2} \right|^k}{q_{e0}} < 0, \\
\dot{V}_3 = \dfrac{2\sum_{i=1}^{3}\left| a\left(|q_{ebi}|^2\right)^{p+1/k/2} + b\left(|q_{ebi}|^2\right)^{g+1/k/2} \right|^k}{q_{e0}} > 0.
\end{cases}
\tag{42}
$$

Equation (42) indicates that $q_{e0} = 1$ is the equilibrium point and $q_{e0} = -1$ is the nonequilibrium point. Similarly, when $q_{e0}(0) < 0$, $\dot{V}_2 > 0$, and $V_3 < 0$ hold, i.e., $q_{e0} = -1$ is the equilibrium point, and $q_{e0} = 1$ is the nonequilibrium point. This completes the proof of Theorem 10.

Furthermore, the proposed QFNFTSMS has a faster convergence performance than other sliding mode surfaces, such as the nonsingular TSM surface [21] and the sliding mode surfaces used in [26–28], as listed below.

$$
\begin{aligned}
s_1 &= q_{eb} + \sigma_1 \operatorname{sig}^{n_1}(\dot{q}_{eb}), \\
s_2 &= q_{eb} + \sigma_2 \operatorname{sig}^{n_2}(q_{eb}) + \sigma_3 \operatorname{sig}^{n_3}(\dot{q}_{eb}), \\
s_3 &= \dot{q}_{eb} + \sigma_4 \operatorname{sig}^{n_4}(q_{eb}) + \sigma_5 \operatorname{sig}^{n_5}(q_{eb}),
\end{aligned}
\tag{43}
$$

where $\sigma_i > 0$, $i = 1, 2, \cdots, 5$, $1 < n_i < 2$, $i = 1, 3$, $n_2 > n_3$, $n_4 > 1$, and $0 < n_5 < 1$ hold. In order to make the sliding mode surfaces have the same coefficients and exponents, the sliding mode surface parameters are selected as follows.

$$
\begin{aligned}
&\sigma_1 = \sigma_3, n_1 = n_3, \sigma_4 = {}^{1/n_3}, n_4 = \frac{n_2}{n_3}, \\
&\sigma_5 = \sigma_3{}^{-1/n_3}, pk = n_5 = n_3{}^{-1}, a = \sigma_5{}^{1/k}, b = \sigma_4{}^{1/k}, gk = n_4.
\end{aligned}
\tag{44}
$$

Based on s_1, we can derive that

$$
\dot{q}_{ebi} = -\left| \frac{q_{ebi}}{\sigma_1} \right|^{1/n_1} \operatorname{sgn}(q_{ebi}).
\tag{45}
$$

Define $y = |q_{ebi}|$, $dt = -\sigma_1{}^{1/n_1}y^{-1/n_1}dy$ holds. Therefore, the convergence time of s_1 can be solved as follows.

$$
T_{s1} = \int_0^{y(0)} \left(\frac{1}{\sigma_1} y \right)^{-1/n_1} dy,
\tag{46}
$$

where $y(0) = |q_{ebi}(0)|$. Similarly, the convergence time of the others can be solved as follows.

$$
\begin{aligned}
T_{s2} &= \int_0^{y(0)} \frac{1}{\left((1/\sigma_3)y + (\sigma_2/\sigma_3)y^{n_2}\right)^{1/n_3}} dy, \\
T_{s3} &= \int_0^{y(0)} \frac{1}{\sigma_4 y^{n_4} + \sigma_5 y^{n_5}} dy, \quad T_s = \int_0^{y(0)} \frac{1}{\left(ay^p + by^g\right)^k} dy.
\end{aligned}
\tag{47}
$$

Combining Equation (44) and Lemma 6, one has

$$
\begin{aligned}
\left(\frac{1}{\sigma_3}y + \frac{\sigma_2}{\sigma_3}y^{n_2} \right)^{1/n_3} &= \left(\frac{1}{\sigma_1}y + \frac{\sigma_2}{\sigma_1}y^{n_2} \right)^{1/n_1} > \left(\frac{1}{\sigma_1}y \right)^{1/n_1}, \\
\left(\frac{1}{\sigma_3}y + \frac{\sigma_2}{\sigma_3}y^{n_2} \right)^{1/n_3} &\leq \left(\frac{1}{\sigma_3} \right)^{1/n_3}y^{1/n_3} + \left(\frac{\sigma_2}{\sigma_3} \right)^{1/n_3}y^{n_2/n_3} \\
&= \sigma_4 y^{n_4} + \sigma_5 y^{n_5} = a^k y^{pk} + b^k y^{gk} \\
&\leq \left(ay^p + by^g\right)^k.
\end{aligned}
\tag{48}
$$

Which implies $T_s \leq T_{s3} \leq T_{s2} < T_{s1}$. With the parameters chosen as $\sigma_1 = \sigma_2 = 1$, $n_1 = 1.5$, $n_2 = 2$, and $k = 2$, the convergence time comparison for different sliding mode surfaces is
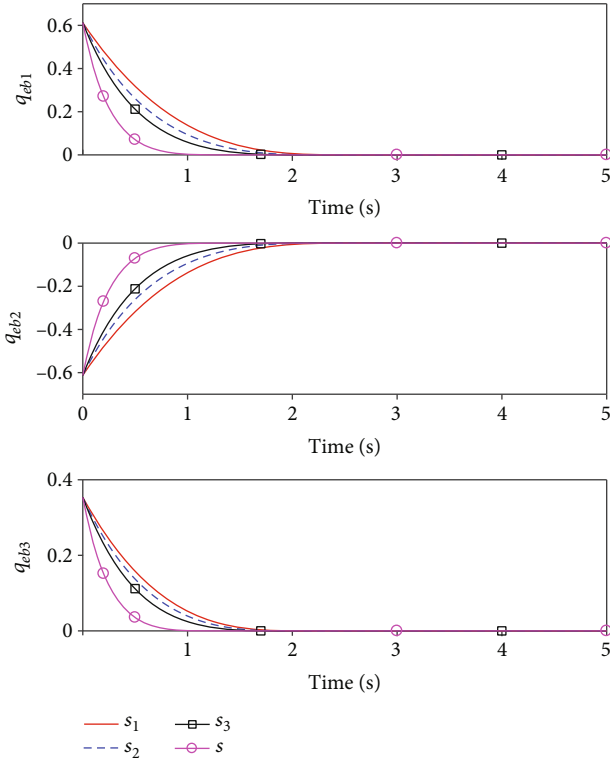
FIGURE 5: Convergence time comparison.

shown in Figure 5, indicating that the proposed QFNFTSMS has a faster convergence performance.

Remark 11. It should be noted that the proposed QFNFTSMS is modified with respect to [29]. In addition to the faster convergence performance proved above, the proposed QFNFTSMS can avoid the singularity without any extra structure. Furthermore, compared with Euler angles used for attitude representation in [34], quaternion has the advantage of avoiding singularity in the kinematic equations. However, the sliding mode surface designed by q_{eb} and $\dot{q}_{eb}$ in [21, 31] and the conclusion that $q_{e0} = -1$ is nonequilibrium point in [17] are both misquoted, whose premise is that the sliding mode surface needs to be designed by q_{eb} and ω_e. In this paper, Theorem 10 provides a complete proof, whose premise is that $q_{e0}(0)$ should not be equal to zero.

3.4.2. Fixed-Time Controller. In this section, a novel quaternion-based fixed-time nonsingular fast terminal sliding mode control law is designed as follows.

$$
\begin{aligned}
u = & -\frac{1}{r_2} B^{-1} \left[\bar{K}(q_{eb}) + K(q_{eb}) \right] sig^{2-r_2}(\dot{q}_{eb}) - B^{-1} h \\
& - \frac{1}{r_2} B^{-1} \operatorname{diag} \left\{ \kappa \left(|\dot{q}_{eb}|^{r_2-1} \right) \right\} \operatorname{diag} \left\{ |\dot{q}_{eb}|^{1-r_2} \right\} \\
& \times sig^{k_1} \left(\alpha sig^{p_1}(s) + \beta sig^{g_1}(s) \right) \\
& - B^{-1} \rho \operatorname{sign}(s) - B^{-1} Z_2,
\end{aligned}
\tag{49}
$$

where $k_1 > 1$, $0 < p_1 k_1 < 1$, $1 < g_1 k_1 < 2k_1 - 1$, $\alpha > 0$, $\beta > 0$, and $\rho > 0$. κ is a nonlinear function defined as follows.

$$
\kappa = \begin{cases} \sin \left(\dfrac{\pi x^2}{2\tau^2} \right) & |x| < \tau, \\ 1 & |x| \geq \tau, \end{cases}
\tag{50}
$$

where τ is a sufficiently small positive number. $\bar{K}(q_{eb})$ is a diagonal matrix, and the diagonal elements $\bar{k}(q_{ebi})(i = 1, 2, 3)$ are denoted as

$$
\begin{aligned}
\bar{k}(q_{ebi}) = & kr_2 \left(a|q_{ebi}|^{p-1/(kr_2)} + b|q_{ebi}|^{g-1/(kr_2)} \right)^{kr_2-1} \\
& \times \left(a \left(p - \frac{1}{kr_2} \right) |q_{ebi}|^{p-1/(kr_2)} \right. \\
& \left. + b \left(g - \frac{1}{kr_2} \right) |q_{ebi}|^{g-1/(kr_2)} \right).
\end{aligned}
\tag{51}
$$

Theorem 12. *For dynamic model (27), with the proposed FESO (32), the proposed QFNFTSMS (35), and the proposed QFNFTSMC (49), q_{eb} and $\dot{q}_{eb}$ can converge to the origin uniformly within fixed time T in spite of the initial conditions, and the upper bound of convergence time T satisfies.*

$$
T \leq T_o + T_c + T_s,
\tag{52}
$$

where T_c satisfies

$$
\begin{aligned}
T_c \leq & \frac{2}{3^{1-k_1} \alpha^{k_1} 2^{(p_1 k_1 + 1)/2} (1 - p_1 k_1)} \\
& + \frac{2}{3^{1-k_1} \beta^{k_1} 2^{(g_1 k_1 + 1)/2} (g_1 k_1 - 1)} + \frac{2\tau^{1/(r_2-1)}}{\rho}.
\end{aligned}
\tag{53}
$$

Proof. Let the positive Lyapunov function be $V_4 = s^T s/2$, then, the derivative of V_4 is obtained as follows.

$$
\begin{aligned}
\dot{V}_4 = & s^T \left[\bar{K}(q_{eb}) + K(q_{eb}) \right] \dot{q}_{eb} \\
& + s^T r_2 \operatorname{diag} \left\{ |\dot{q}_{eb}|^{r_2-1} \right\} (h + Bu + D).
\end{aligned}
\tag{54}
$$

Substituting Equation (49) into Equation (54), we can get

$$
\begin{aligned}
\dot{V}_4 = & -s^T \operatorname{diag} \left\{ \kappa \left(|\dot{q}_{eb}|^{r_2-1} \right) \right\} sig^{k_1} \left(\alpha sig^{p_1}(s) + \beta sig^{g_1}(s) \right) \\
& + s^T r_2 \operatorname{diag} \left\{ |\dot{q}_{eb}|^{r_2-1} \right\} (-\rho \operatorname{sgn}(s) - Z_2 + D).
\end{aligned}
\tag{55}
$$

Because $Z_2 \longrightarrow D$ within a fixed time T_o, Equation (55) can be simplified as follows.

$$\dot{V}_4 < -s^T \, \text{diag} \left\{ \kappa \left(|\dot{q}_{eb}|^{r_2-1} \right) \right\} sig^{k_1} (\alpha sig^{p_1}(s) + \beta sig^{g_1}(s))$$

$$\leq -3^{1-k_1} \left(\begin{array}{c} \alpha \min \left(\kappa_i^{1/k_1} \right) \sum\limits_{i=1}^{3} \left(|s_i|^2 \right)^{p_1 k_1 + 1/2k_1} \\ + \beta \min \left(\kappa_i^{1/k_1} \right) \sum\limits_{i=1}^{3} \left(|s_i|^2 \right)^{g_1 k_1 + 1/2k_1} \end{array} \right)^{k_1}$$

$$\leq - \left(\begin{array}{c} 3^{(1-k_1)/k_1} \alpha \min \left(\kappa_i^{1/k_1} \right) 2^{(p_1 k_1 + 1)/(2k_1)} V^{(p_1 k_1 + 1)/(2k_1)} \\ + 3^{(1-k_1)/k_1} \beta \min \left(\kappa_i^{1/k_1} \right) 2^{(g_1 k_1 + 1)/(2k_1)} V^{(g_1 k_1 + 1)/(2k_1)} \end{array} \right)^{k_1}$$

$$\leq - \left(\begin{array}{c} \alpha_m \min \left(\kappa_i^{1/k_1} \right) V^{(p_1 k_1 + 1)/(2k_1)} \\ + \beta_m \min \left(\kappa_i^{1/k_1} \right) V^{(g_1 k_1 + 1)/(2k_1)} \end{array} \right)^{k_1},$$

(56)

where α_m and β_m are defined as

$$\alpha_m = 3^{(1-k_1)/k_1} \alpha 2^{(p_1 k_1 + 1)/(2k_1)}, \beta_m = 3^{(1-k_1)/k_1} \beta 2^{(g_1 k_1 + 1)/(2k_1)}.$$

(57)

The state space is divided into two areas as

$$\delta_1 = \left\{ (q_{ebi}, \dot{q}_{ebi}) \big| |\dot{q}_{ebi}|^{r_2-1} \geq \tau, \forall i = 1, 2, 3 \right\},$$
$$\delta_2 = \left\{ (q_{ebi}, \dot{q}_{ebi}) \big| |\dot{q}_{ebi}|^{r_2-1} < \tau, \exists i = 1, 2, 3 \right\}.$$

(58)

□

When the system states q_{eb} and $\dot{q}_{eb}$ are in the region δ_1, $|\dot{q}_{ebi}| \geq \tau^{1/(r_2-1)}, \forall i = 1, 2, 3$ and $\min (\kappa_i^{1/k_1}) = 1$ satisfies, so $\dot{V} \leq -(\alpha_m V^{(p_1 k_1 + 1)/(2k_1)} + \beta_m V^{(g_1 k_1 + 1)/(2k_1)})^{k_1}$, therefore, system states q_{eb} and $\dot{q}_{eb}$ will be driven on the sliding mode surface $s = 0$ or into the region δ_2 in fixed convergence time T_{c1} based on Lemma 5. Where T_{c1} satisfies

$$T_{c1} \leq \frac{2}{3^{1-k_1} \alpha^{k_1} 2^{(p_1 k_1 + 1)/2} (1 - p_1 k_1)} + \frac{2}{3^{1-k_1} \beta^{k_1} 2^{(g_1 k_1 + 1)/2} (g_1 k_1 - 1)}.$$

(59)

If the system states q_{eb} and $\dot{q}_{eb}$ are in the region δ_2, i.e., $0 \leq |\dot{q}_{ebi}| < \tau^{1/(r_2-1)}, \exists i = 1, 2, 3$ holds. When $|\dot{q}_{ebi}| \neq 0, \forall i = 1, 2, 3$, it can also be verified that $s = 0$ is still an attractor. When $\dot{q}_{ebi} = 0, \exists i = 1, 2, 3$, combined with Equation (27) and Equation (49), we can get $\ddot{q}_{ebi} = -\rho \, \text{sgn}(s_i)$, if $s_i > 0$, then $\ddot{q}_{ebi} = -\rho < 0$, if $s_i < 0$, then $\ddot{q}_{ebi} = \rho > 0$. Therefore, $\dot{q}_{ebi} = 0$ is not an attractor except for the origin. Furthermore, assuming that $\ddot{q}_{ebi} = -\rho \, \text{sgn}(s_i)$ holds approximately when $|\dot{q}_{ebi}| < \tau^{1/(r_2-1)}$, the system states will pass through the region δ_2 monotonically in fixed time T_{c2}, where $T_{c2} \leq 2\tau^{1/(r_2-1)}/\rho$. So, system states q_{eb} and $\dot{q}_{eb}$ will be driven on the sliding mode surface $s = 0$ within fixed time $T_c = T_{c1} + T_{c2}$. Then, combined with the observer convergence time T_o and the

sliding mode surface convergence time T_s, Theorem 12 is proved.

Remark 13. It should be noted that the control law (49) is modified with respect to [29, 34]. Because the unknown disturbance can be estimated by the fixed-time observer, the proposed control law does not require the disturbance boundary in advance. Compared with the controller proposed in [34], the disturbance effect on the satellite system can be offset by feeding back Z_2 to improve control accuracy and the stability condition for $\rho \geq 0$, which greatly reduces the parameter selection range to attenuate the chattering. In this paper, in order to enable the system state to pass through the region δ_2, ρ is selected as a small constant greater than zero, and then a saturation function is used to achieve chattering-free attitude control.

4. Simulation Results

4.1. Disturbance Effect. In this section, the lumped disturbance simulation results when Assumption 1 and Assumption 2 do not hold are given, then the AMB mechanical characteristics are determined, and finally, the effects of lumped disturbance and uncertainty on the RPS system are discussed. The RPS system parameters are shown in Table 3.

To simulate the imaging phase, initial values of quaternion of the platform subsystem and the payload subsystem are both $[1,0,0,0]^T$, and initial values of angular velocity of the platform subsystem and the payload subsystem are $[0.001,0,0]^T$ rad/s and $[0.001,0,0.28]^T$ rad/s, respectively. The desired angular velocity of the platform subsystem is $\omega_0 = 0.0011$ rad/s, and the expected attitude quaternion of the platform subsystem is $[\cos (\omega_0 t/2), \sin (\omega_0 t/2), 0, 0]^T$. The control method used in this section refers to the PD control method in [37]. The adjusting time and damping ratio of the control system is 10 s and 1, respectively. The uncertainty of inertia parameter is 10%, i.e., $J_{pfn} = 0.9 J_{pf}$. The maximum output of the satellite platform momentum wheel is 1 Nm. In general, the parameter settings in this section are consistent with case 2 in Section 2.

In addition, the stiffness and damping parameters of AMB are considered in two cases. Case A: angle stiffness 2450.5 Nm/rad, angle damping 40546.3 Ns/rad. Case B: angle stiffness 2450.5 Nm/rad, angle damping 810.9 Ns/rad. The relative angular deviation of AMB under the two mechanical characteristics is shown in Figure 6, where the relative angular deviation of case B increases from 0.002 deg to 0.011 deg compared to case A, so Assumption 1 is not accurate in case B. Furthermore, influenced by the disturbance d', the satellite platform control accuracy is low in both cases, so Assumption 2 is not valid in both cases.

The lumped disturbance transmitted by AMB is shown as Figure 7, where the maximum value of case A increases from 0.8007 Nm of theoretical results to 0.8418 Nm, an increase of 5.1%, and the maximum value of case B further increases to 0.8609 Nm, an increase of 7.5%. Therefore, the mechanical characteristics of low stiffness and low damping, i.e., case B, will amplify the lumped disturbance to a certain

TABLE 3: Parameters of the RPS system.

Mass of platform subsystem	$M_{pf} = 1368\text{kg}$
Inertia of platform subsystem	$J_{pf} = \begin{bmatrix} 566.7 & -3.7 & -3.7 \\ -3.7 & 3658.9 & -3.7 \\ -3.7 & -3.7 & 3705.6 \end{bmatrix} \text{kg} \cdot \text{m}^2$
Axial inertia of momentum wheel $i(i = x, y, z)$	$J_{Wi} = 0.052\text{kg} \cdot \text{m}^2$
Mass of payload subsystem	$M_{pl} = 838\text{kg}$
Inertia of payload subsystem	$J_{pl} = \begin{bmatrix} 214.5 & 0 & -3.9 \\ 0 & 211.9 & 0 \\ -3.9 & 0 & 253.3 \end{bmatrix} \text{kg} \cdot \text{m}^2$
Axial inertia of momentum wheel t	$J_{Wt} = 0.362\text{kg} \cdot \text{m}^2$
Static unbalance	$r_j = \begin{bmatrix} 5 & 0 & -9.6 \end{bmatrix}^T \text{mm}$
Dynamic unbalance	$I_{xz} = 3.9\text{kg} \cdot \text{m}^2$
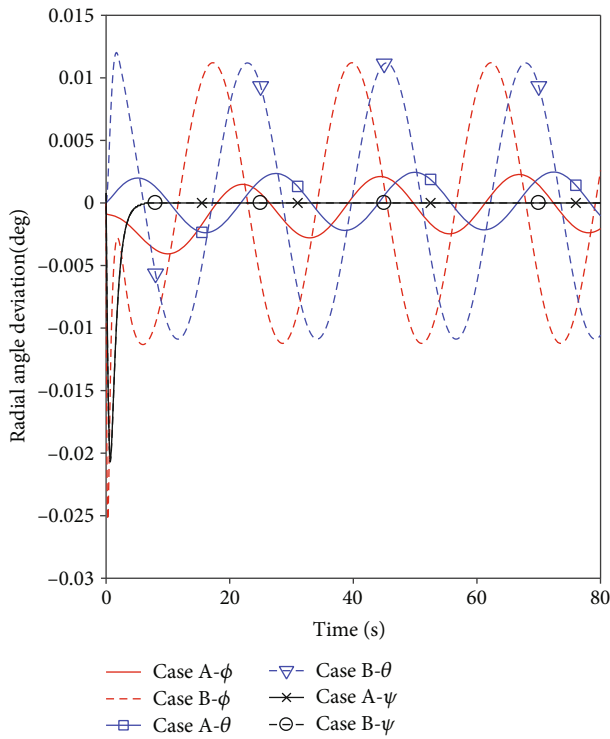
FIGURE 6: Radial angle deviation of AMB.

FIGURE 7: Simulation results of the lumped disturbance.

extent, but the theoretical results still have more than 90% accuracy.

More factors need to be considered in the selection of mechanical characteristics of AMB. The relative angle deviation of low stiffness and low damping is large, as shown in case B of Figure 6, which seriously affects the attitude accuracy and stability of the payload. Meanwhile, increasing stiffness is not conducive to isolating the medium and high-frequency vibration of satellite platform caused by flywheel eccentricity. Therefore, the mechanical characteristics of AMB with low stiffness and high damping, i.e., case A, are finally determined.
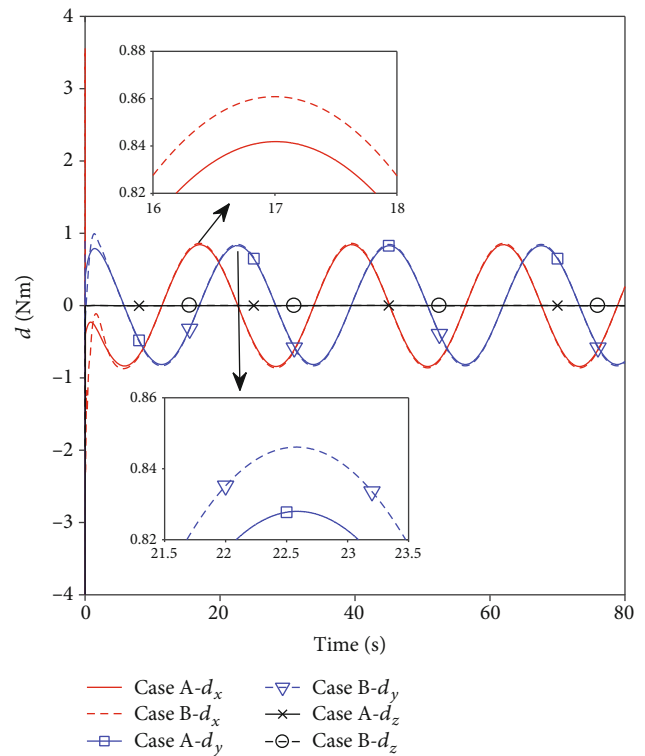
Then, the simulation results of the RPS system attitude under the lumped disturbance and uncertainty are shown in Figure 8. As shown in Figures 8(a), 8(c), and 8(h), the lumped disturbance and uncertainty result in nutation motion of the satellite platform, and the nutation motion tends to be stable in 10 s, in which angle control accuracy is 0.011 deg, and angular velocity control accuracy is 0.0032 deg/s. From Figure 8(d), it can be seen that the control torque tends to be stable in 10 s with an amplitude of 0.85 Nm.

As shown in case A of Figures 6, 8(e), 8(f), and 8(h), the nutation of the payload relative to the platform also exists,
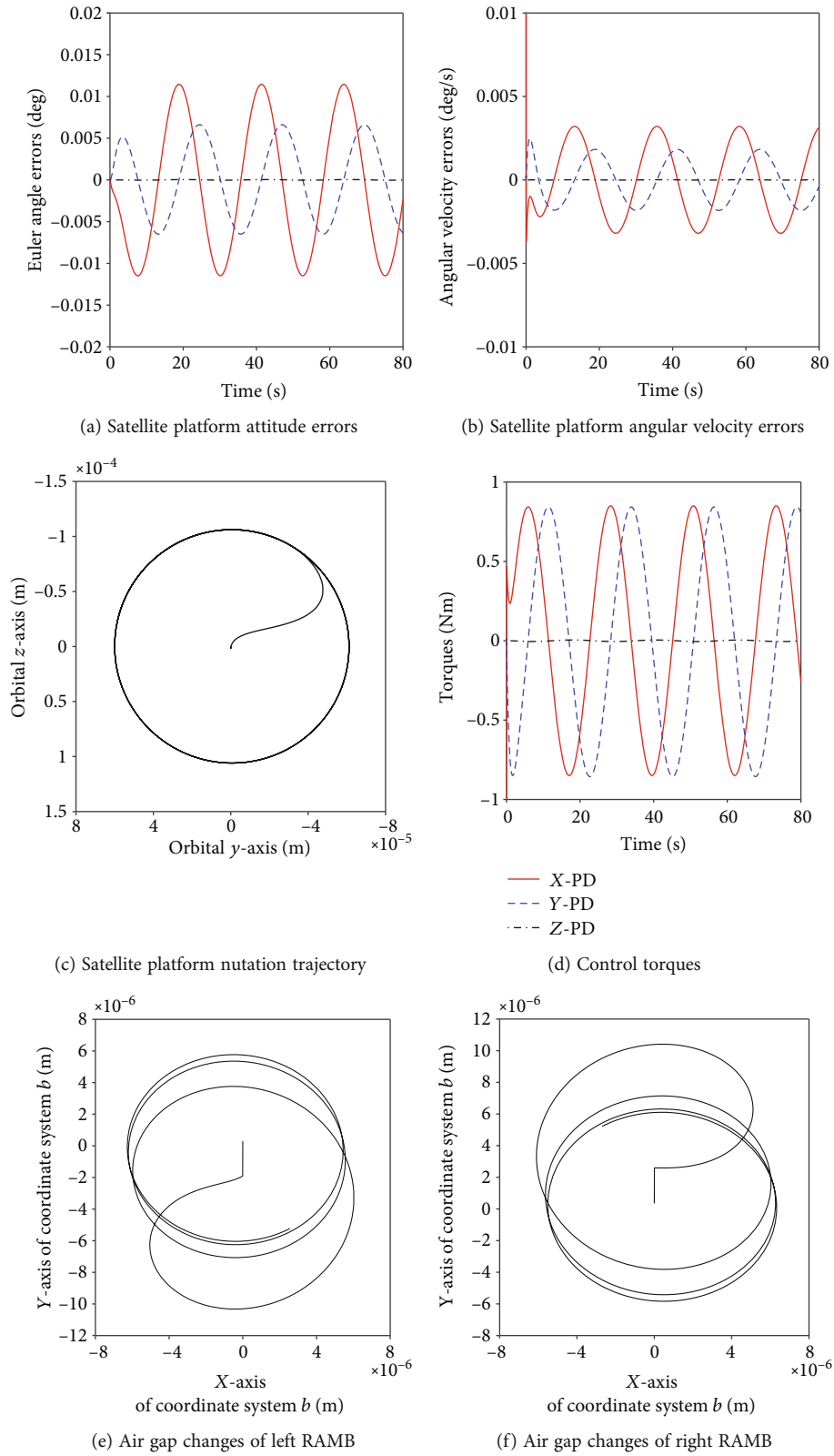
(a) Satellite platform attitude errors

(b) Satellite platform angular velocity errors

(c) Satellite platform nutation trajectory

(d) Control torques

(e) Air gap changes of left RAMB

(f) Air gap changes of right RAMB

Figure 8: Continued.

(g) Payload nutation trajectory

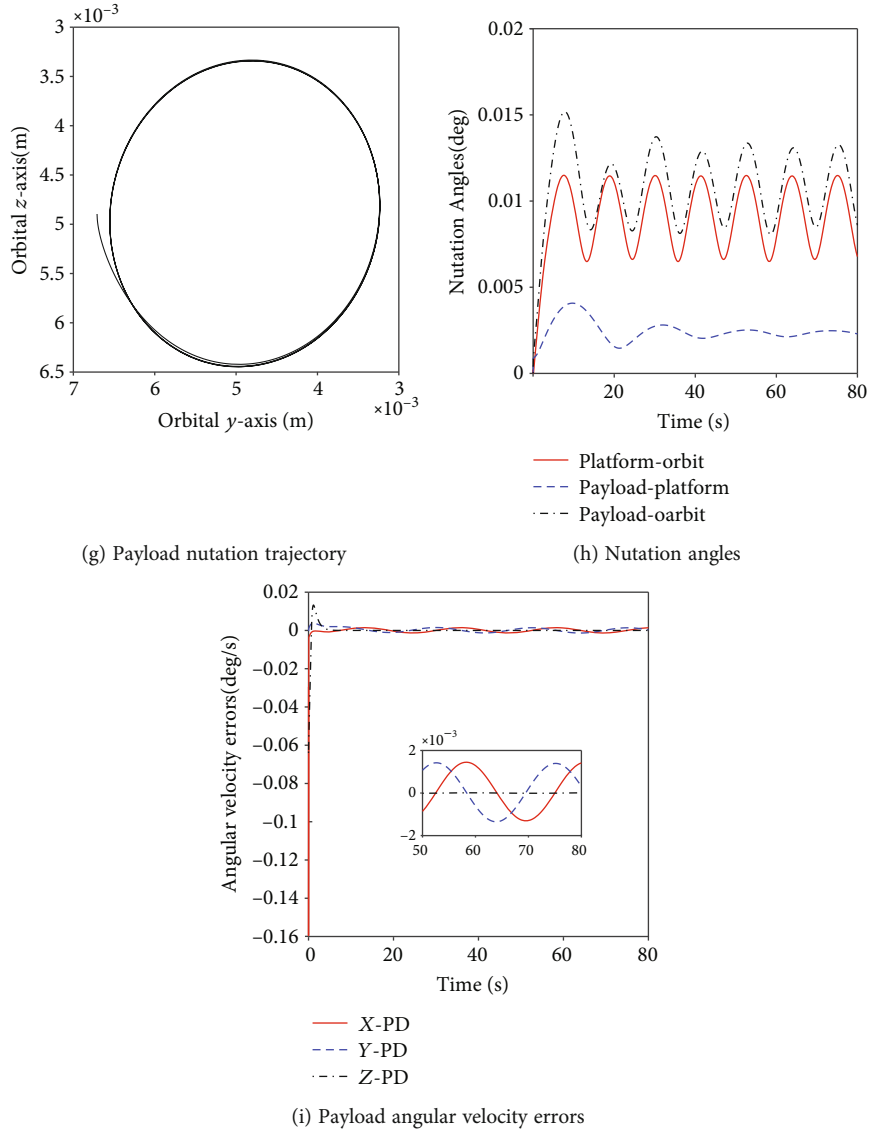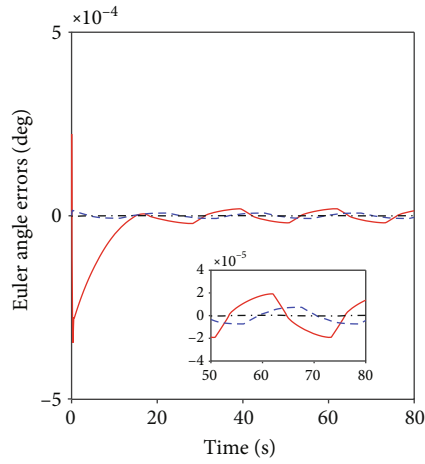(h) Nutation angles

(i) Payload angular velocity errors

FIGURE 8: RPS system attitude results under the lumped disturbance and uncertainty.

wherein the air gap changing ranges of AMB are stable within 6e-6 m. In addition, the change of the air gaps of the left RAMB and right RAMB are symmetric with respect to the AMB's geometric center. Finally, as shown in Figures 8(h) and 8(i), the attitude accuracy and angular velocity accuracy of the payload under the lumped disturbance and uncertainty are 0.014 deg and 0.002 deg/s, respectively, which affect the accuracy of the payload in the imaging phase.

4.2. Fixed-Time Control. In this section, in order to verify the effectiveness of the proposed controller to reject the lumped disturbance and uncertainty effect in the imaging phase, numerical simulation results are presented. The sliding mode surface parameters are selected as follows: $g = 0.7$, $p = 0.4$, $k = 2$, $r_2 = 5/3$, and $a = b = 1.5$. The controller parameters are selected as $p_1 = 1/3$, $g_1 = 3/4$, $k_1 = 1.85$, $\alpha = \beta = 1$, $\tau = 0.005$, and $\rho = 0.0001$. The fixed-time observer parame-

ters are selected as follows: $L = 0.001$, $\zeta = 1.5$, $\lambda_1 = 0.101$, $\lambda_2 = 0.001$, $\lambda_3 = 0.005$, and $Z_1(0) = Z_2(0) = 0^{3\times1}$. And the other parameters refer to Table 3, then, the simulation results of the RPS system attitude under the proposed controller (49) are shown in Figure 9.

As shown in Figures 9(a)–9(c) and 9(h), nutation motion of the satellite platform is suppressed by the proposed fixed-time controller. Compared with Figures 8(a)–8(c), the satellite platform has a higher attitude accuracy and avoids chattering. From Figure 9(d), it can be seen that the control torque tends to be stable in 0.8 Nm without chattering phenomenon. In addition, the sliding mode surface converges to zero within a bounded time, as shown in Figure 9(e). Meanwhile, as shown in Figure 9(f), the estimation error of the fixed-time observer also converges to the neighborhood of zero, which is caused by using the boundary layer method to deal with the chattering problem. This indicates that the disturbance d' is well estimated by the observer.
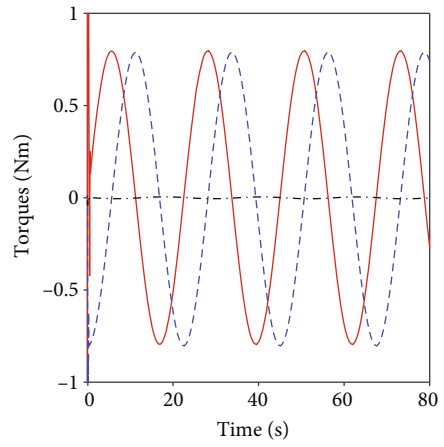
(a) Satellite platform attitude errors
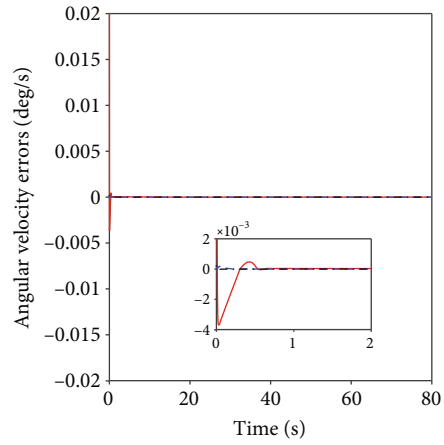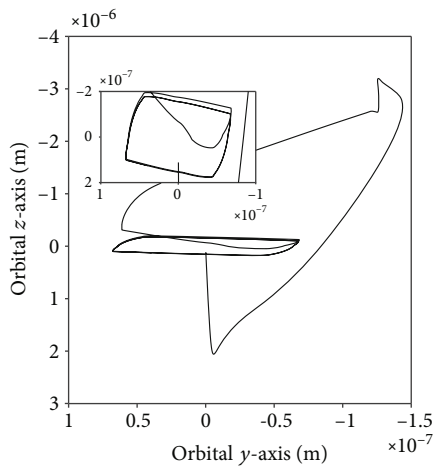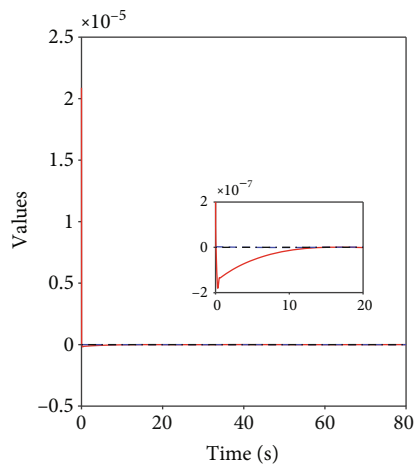

(b) Satellite platform angular velocity errors
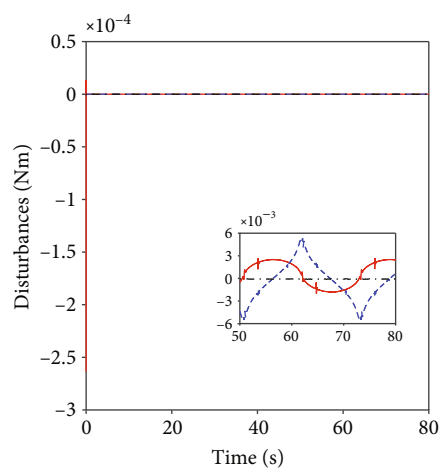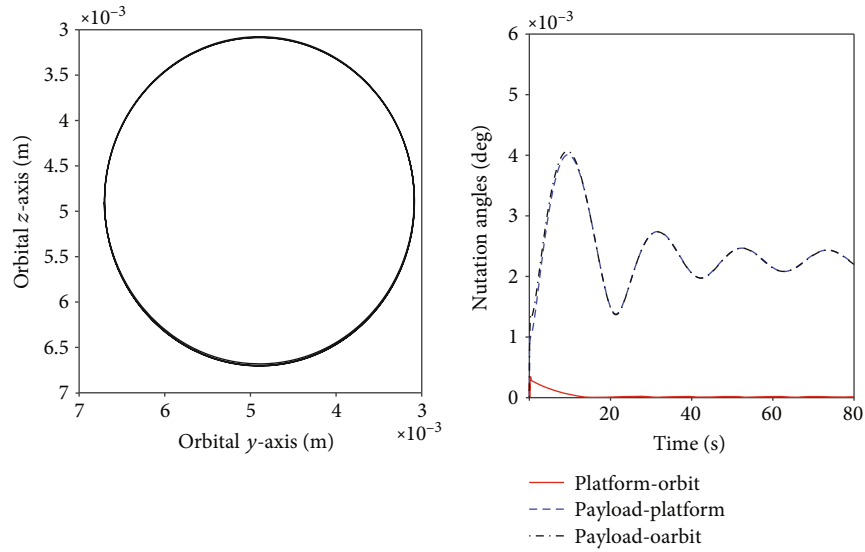

(c) Satellite platform nutation trajectory

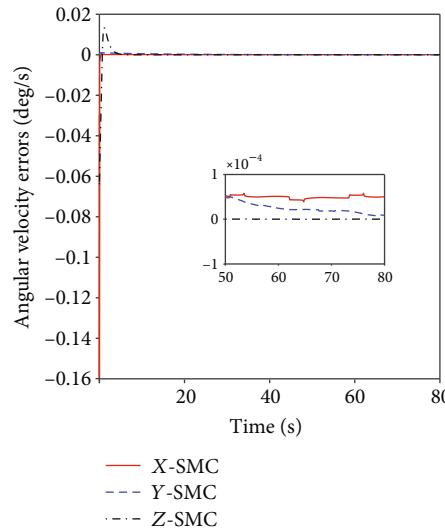(d) Control torques

(e) Sliding mode surface

(f) Estimation errors of observer

Figure 9: Continued.

(g) Payload nutation trajectory

(h) Nutation angles

(i) Payload angular velocity errors

FIGURE 9: RPS system attitude results under the proposed controller.

Then, the nutation of the payload relative to the platform and the air gap changes of AMB under the proposed controller is the same as the PD control and can refer to the previous section. Finally, as shown in Figures 9(h) and 9(i), based on the high precision and high stability attitude control of the platform, the payload nutation is consistent with the nutation motion of the payload relative to the platform. Among them, the nutation angle is stable within 0.003 deg, and the angular velocity accuracy converges to within 0.0001 deg/s. The above simulation results show that the proposed controller has excellent suppression effect on the lumped disturbance and uncertainty, which improves the attitude accuracy and attitude stability of the payload in the imaging phase.

5. Conclusions

In this paper, dynamic model and attitude controller have been studied for the RPS system with a 5-DOF AMB and an unbalanced rotating payload. The dynamic model of the lumped disturbance is established, and the balancing error index of payload unbalance is designed with the maximum torque of actuator as constraint. Subsequently, a disturbance analysis including the effect of AMB mechanical characteristics is carried out, and the simulation results show that the proposed model has more than 90% accuracy in practice, ensuring the effectiveness of the balancing error index. On this basis, a novel QFNFTSMC integrating FESO is proposed in the presence of unknown lumped disturbance and uncertainty. Compared with the previous work, the proposed controller has faster convergence speed, and the disturbance effect is compensated to improve control accuracy and reduce switching gain significantly. Furthermore, the effectiveness of the proposed controller is demonstrated through simulation. Simulation results show that the attitude accuracy and angular velocity accuracy of payload increase from 0.014 deg to 0.003 deg and 0.002 deg/s to

0.0001 deg/s, respectively, which achieves high precision, high stability, and chattering-free attitude control and ensures the imaging quality of the RPS system in the imaging phase.

Data Availability

The data used to support the findings of this study are included within the article.

Conflicts of Interest

The authors declare that there is no conflict of interest regarding the publication of this paper.

References

[1] X. Tang, F. Hu, M. Wang, J. Pan, S. Jin, and G. Lu, "Inner FoV stitching of spaceborne TDI CCD images based on sensor geometry and projection plane in object space," *Remote Sensing*, vol. 6, no. 7, pp. 6386–6406, 2014.

[2] Y. Lu, K. Wang, and G. Fan, "Photometric calibration and image stitching for a large field of view multi-camera system," *Sensors*, vol. 16, no. 4, p. 516, 2016.

[3] H. Afshari, V. Popovic, T. Tasci, A. Schmid, and Y. Leblebici, "A spherical multi-camera system with real-time omnidirectional video acquisition capability," *IEEE Transactions on Consumer Electronics*, vol. 58, no. 4, pp. 1110–1118, 2012.

[4] F. Wu, X. Cao, E. A. Butcher, and F. Wang, "Dynamics and control of spacecraft with a large misaligned rotational component," *Aerospace Science and Technology*, vol. 87, pp. 207–217, 2019.

[5] Y. Xu, J. Zhou, and C. Jin, "Identification of dynamic stiffness and damping in active magnetic bearings using transfer functions of electrical control system," *Journal of Mechanical Science and Technology*, vol. 33, no. 2, pp. 571–577, 2019.

[6] I. Valiente-Blanco, E. Diez-Jimenez, C. Cristache, M. A. Alvarez-Valenzuela, and J. L. Perez-Diaz, "Characterization and improvement of axial and radial stiffness of contactless thrust superconducting magnetic bearings," *Tribology Letters*, vol. 54, no. 3, pp. 213–220, 2014.

[7] Y. Zhao, X. Chen, F. Wang, C. Wei, and Y. Zhao, "Modeling of active magnetic bearing in rotating payload satellite considering shaft motion coupling," *Journal of Mechanical Science and Technology*, vol. 34, no. 11, pp. 4423–4437, 2020.

[8] W. A. Oke, M. A. Abido, and T. B. Asafa, "Balancing of flexible rotors based on evolutionary algorithms," *Mechanics & Industry*, vol. 16, no. 4, p. 406, 2015.

[9] P. Iannelli, F. Angeletti, and P. Gasbarri, *An Attitude/Spin Control Architecture for a Spacecraft Equipped with a Flexible Rotating Payload Based on Model Predictive Control*, Presented at the International Astronautical Congress, Dubai, 2021.

[10] S. Sun, C. Wei, Z. Huang et al., "Adaptive control of space robot despinning tumbling target using flexible brushes," *International Journal of Aerospace Engineering*, vol. 2021, Article ID 6196556, 9 pages, 2021.

[11] X. Jia, L. Hu, F. Feng, and J. Xu, "Robust H infinity consensus control for linear discrete-time swarm systems with parameter uncertainties and time-varying delays," *International Journal of Aerospace Engineering*, vol. 2019, Article ID 7278531, 16 pages, 2019.

[12] S. Shen and J. Xu, "Attitude active disturbance rejection control of the quadrotor and its parameter tuning," *International Journal of Aerospace Engineering*, vol. 2020, Article ID 8876177, 15 pages, 2020.

[13] H. Zhuang, Q. Sun, Z. Chen, and X. Zeng, "Back-stepping active disturbance rejection control for attitude control of aircraft systems based on extended state observer," *International Journal of Control, Automation and Systems*, vol. 19, no. 6, pp. 2134–2149, 2021.

[14] Y. P. Chen and S. C. Lo, "Sliding-mode controller design for spacecraft attitude tracking maneuvers," *IEEE Transactions on Aerospace and Electronic Systems*, vol. 29, no. 4, pp. 1328–1333, 1993.

[15] Q. Hu, Z. Wang, and H. Gao, "Sliding mode and shaped input vibration control of flexible systems," *IEEE Transactions on Aerospace and Electronic Systems*, vol. 44, no. 2, pp. 503–519, 2008.

[16] R. Sun, J. Wang, D. Zhang, and X. Shao, "Neural-network-based sliding-mode adaptive control for spacecraft formation using aerodynamic forces," *Journal of Guidance, Control, and Dynamics*, vol. 41, no. 3, pp. 757–763, 2018.

[17] E. Jin and Z. Sun, "Robust controllers design with finite time convergence for rigid spacecraft attitude tracking control," *Aerospace Science and Technology*, vol. 12, no. 4, pp. 324–330, 2008.

[18] Z. Zhu, Y. Xia, and M. Fu, "Attitude stabilization of rigid spacecraft with finite-time convergence," *International Journal of Robust and Nonlinear Control*, vol. 21, no. 6, pp. 686–702, 2011.

[19] J. Qiao, D. Zhang, Y. Zhu, and P. Zhang, "Disturbance observer-based finite-time attitude maneuver control for micro satellite under actuator deviation fault," *Aerospace Science and Technology*, vol. 82, pp. 262–271, 2018.

[20] Z. Song, H. Li, and K. Sun, "Finite-time control for nonlinear spacecraft attitude based on terminal sliding mode technique," *ISA Transactions*, vol. 53, no. 1, pp. 117–124, 2014.

[21] K. Lu and Y. Xia, "Finite-time fault-tolerant control for rigid spacecraft with actuator saturations," *IET Control Theory Applications*, vol. 7, no. 11, pp. 1529–1539, 2013.

[22] Q. Hu and B. Jiang, "Continuous finite-time attitude control for rigid spacecraft based on angular velocity observer," *IEEE Transactions on Aerospace and Electronic Systems*, vol. 54, no. 3, pp. 1082–1092, 2018.

[23] A. Zou, K. D. Kumar, Z. Hou, and X. Liu, "Finite-time attitude tracking control for spacecraft using terminal sliding mode and Chebyshev neural network," *IEEE Transactions on Systems, Man, and Cybernetics, Part B (Cybernetics)*, vol. 41, no. 4, pp. 950–963, 2011.

[24] K. Lu and Y. Xia, "Adaptive attitude tracking control for rigid spacecraft with finite-time convergence," *Automatica*, vol. 49, no. 12, pp. 3591–3599, 2013.

[25] Q. Shen, D. Wang, S. Zhu, and K. Poh, "Finite-time fault-tolerant attitude stabilization for spacecraft with actuator saturation," *IEEE Transactions on Aerospace and Electronic Systems*, vol. 51, no. 3, pp. 2390–2405, 2015.

[26] L. Yang and J. Yang, "Nonsingular fast terminal sliding-mode control for nonlinear dynamical systems," *International Journal of Robust and Nonlinear Control*, vol. 21, no. 16, pp. 1865–1879, 2011.

[27] J. Wang, C. Liu, Y. Wang, and G. Zheng, "Fixed time integral sliding mode controller and its application to the suppression of chaotic oscillation in power system," *Chinese Physics B*, vol. 27, no. 7, p. 070503, 2018.

[28] H. Li and Y. Cai, "On SFTSM control with fixed-time convergence," *IET Control Theory & Applications*, vol. 11, no. 6, pp. 766–773, 2017.

[29] Y. Huang and Y. Jia, "Fixed-time consensus tracking control for second-order multi-agent systems with bounded input uncertainties via NFFTSM," *IET Control Theory & Applications*, vol. 11, no. 16, pp. 2900–2909, 2017.

[30] C. Wu, J. Yan, H. Lin, X. Wu, and B. Xiao, "Fixed-time disturbance observer-based chattering-free sliding mode attitude tracking control of aircraft with sensor noises," *Aerospace Science and Technology*, vol. 111, p. 106565, 2021.

[31] Q. Chen, S. Xie, M. Sun, and X. He, "Adaptive nonsingular fixed-time attitude stabilization of uncertain spacecraft," *IEEE Transactions on Aerospace and Electronic Systems*, vol. 54, no. 6, pp. 2937–2950, 2018.

[32] B. Jiang, Q. Hu, and M. I. Friswell, "Fixed-time attitude control for rigid spacecraft with actuator saturation and faults," *IEEE Transactions on Control Systems Technology*, vol. 24, no. 5, pp. 1892–1898, 2016.

[33] L. Zhang, C. Wei, R. Wu, and N. Cui, "Fixed-time extended state observer based non-singular fast terminal sliding mode control for a VTVL reusable launch vehicle," *Aerospace Science and Technology*, vol. 82–83, pp. 70–79, 2018.

[34] L. Zhang, C. Wei, L. Jing, and N. Cui, "Fixed-time sliding mode attitude tracking control for a submarine-launched missile with multiple disturbances," *Nonlinear Dynamics*, vol. 93, no. 4, pp. 2543–2563, 2018.

[35] M. Basin, C. B. Panathula, and Y. Shtessel, "Multivariable continuous fixed-time second-order sliding mode control: design and convergence time estimation," *IET Control Theory & Applications*, vol. 11, no. 8, pp. 1104–1111, 2016.

[36] M. Basin, P. Rodriguez-Ramirez, and A. Garza-Alonso, "Continuous fixed-time convergent super-twisting algorithm in case of unknown state and disturbance initial conditions: continuous fixed-time convergent super-twisting algorithm," *Asian Journal of Control*, vol. 21, no. 1, pp. 323–338, 2019.

[37] B. Wie, H. Weiss, and A. Arapostathis, "Quarternion feedback regulator for spacecraft eigenaxis rotations," *Journal of Guidance, Control, and Dynamics*, vol. 12, no. 3, pp. 375–380, 1989.